


# Microtubule poleward flux in human cells is driven by the coordinated action of four kinesins

Yulia Steblyanko<sup>1</sup>, Girish Rajendraprasad<sup>1</sup>, Mariana Osswald<sup>2,3</sup>, Susana Eibes<sup>1</sup>, Ariana Jacome<sup>2,3</sup>, Stephan Geley<sup>4</sup>, António J Pereira<sup>2,3</sup>, Helder Maiato<sup>2,3,5</sup> & Marin Barisic<sup>1,6,\*</sup> 

## Abstract

Mitotic spindle microtubules (MTs) undergo continuous poleward flux, whose driving force and function in humans remain unclear. Here, we combined loss-of-function screenings with analysis of MT-dynamics in human cells to investigate the molecular mechanisms underlying MT-flux. We report that kinesin-7/CENP-E at kinetochores (KTs) is the predominant driver of MT-flux in early prometaphase, while kinesin-4/KIF4A on chromosome arms facilitates MT-flux during late prometaphase and metaphase. Both these activities work in coordination with kinesin-5/EG5 and kinesin-12/KIF15, and our data suggest that the MT-flux driving force is transmitted from non-KT-MTs to KT-MTs by the MT couplers HSET and NuMA. Additionally, we found that the MT-flux rate correlates with spindle length, and this correlation depends on the establishment of stable end-on KT-MT attachments. Strikingly, we find that MT-flux is required to regulate spindle length by counteracting kinesin 13/MCAK-dependent MT-depolymerization. Thus, our study unveils the long-sought mechanism of MT-flux in human cells as relying on the coordinated action of four kinesins to compensate for MT-depolymerization and regulate spindle length.

**Keywords** kinesins; kinetochore; microtubules; mitosis; mitotic spindle

**Subject Categories** Cell Adhesion, Polarity & Cytoskeleton; Cell Cycle

**DOI** 10.15252/emboj.2020105432 | Received 27 April 2020 | Revised 24

September 2020 | Accepted 25 September 2020 | Published online 19 October 2020

The EMBO Journal (2020) 39: e105432

## Introduction

Microtubule (MT) poleward flux is an evolutionarily conserved process in metazoan spindles and is defined as a continuous poleward motion of MTs, typically coordinated with addition of new tubulin subunits at the MT plus-ends and their removal at the MT minus-ends at spindle poles (Forer, 1965; Bajer & Molè-Bajer, 1972;

Hiramoto & Izutsu, 1977; Hamaguchi *et al*, 1987; Mitchison, 1989). Although its functions remain unclear, MT-flux was proposed to play a role in various aspects of mitosis. For instance, MT-flux has been implicated in the regulation of spindle length (Gaetz & Kapoor, 2004; Rogers *et al*, 2004; Fu *et al*, 2015; Renda *et al*, 2017). However, this role remains controversial, as attenuation of MT-flux led to spindle elongation in *Drosophila* embryos (Rogers *et al*, 2004) and *Xenopus* egg extracts (Gaetz & Kapoor, 2004), while its reduction in human cells either had no effect on spindle length (Ganem *et al*, 2005; Jiang *et al*, 2017), or resulted in shorter spindles (Maffini *et al*, 2009; Fu *et al*, 2015). Additionally, MT-flux was proposed to regulate kinetochore (KT) activity (Maddox *et al*, 2003) and chromosome movements (Rogers *et al*, 2004; Ganem *et al*, 2005), mediate the correction of erroneous KT-MT attachments (Ganem *et al*, 2005), and equalize spindle forces at metaphase KT prior to their segregation (Matos *et al*, 2009).

In addition to its unclear function, the molecular mechanism underlying MT-flux also remains controversial. Two main models were proposed to drive spindle MT-flux. The first model envisions MT-flux to be driven by kinesin-13-induced depolymerization of MT minus-ends at the spindle poles (Rogers *et al*, 2004; Ganem *et al*, 2005). However, several lines of evidence have challenged this model. In particular, fluorescence speckle microscopy in newt lung cells showed no flux in astral MTs (Waterman-Storer *et al*, 1998), which originate at the poles and extend toward the cell cortex. Moreover, laser microsurgery experiments on KT-MTs (also called k-fibers) revealed normal MT-flux despite stable MT minus-ends detached from the spindle poles (Maiato *et al*, 2004; Matos *et al*, 2009). Finally, MTs continued to flux at unchanged rates even when MT-depolymerization at spindle poles was inhibited by controlled mechanical compression applied to metaphase mitotic spindles (Dumont & Mitchison, 2009). Together, these experiments demonstrate that MT-flux can be uncoupled from MT minus-end depolymerization.

The second model proposes that MT-depolymerization (and polymerization) are a response to kinesin-5-mediated sliding of antiparallel interpolar MTs (Brust-Mascher & Scholey, 2002; Miyamoto

1 Danish Cancer Society Research Center (DCRC), Copenhagen, Denmark

2 i3S - Instituto de Investigação e Inovação em Saúde, Universidade do Porto, Porto, Portugal

3 IBMC - Instituto de Biologia Molecular e Celular, Universidade do Porto, Porto, Portugal

4 Institute of Pathophysiology, Biocenter, Medical University of Innsbruck, Innsbruck, Austria

5 Experimental Biology Unit, Department of Biomedicine, Faculdade de Medicina, Universidade do Porto, Porto, Portugal

6 Department of Cellular and Molecular Medicine, Faculty of Health Sciences, University of Copenhagen, Copenhagen, Denmark

\*Corresponding author. Tel. +45 35257323; E-mail: barisic@cancer.dk

et al, 2004; Matos et al, 2009; Pereira & Maiato, 2012), which could then be translated from interpolar- to KT-MTs via MT crosslinking molecules (Shimamoto et al, 2011; Vladimirova et al, 2013). However, this mechanism was challenged by experiments showing that inhibition of kinesin-5 (EG5 in humans) only slightly reduced MT-flux rates both in bipolar and monopolar spindles (Cameron et al, 2006). Moreover, the ability of monopolar spindles to flux (Cameron et al, 2006) further suggests that antiparallel interpolar MTs do not play an essential role in this process in mammalian cells.

Thus, although MT-flux has been studied over three decades, the molecular mechanisms underlying spindle MT-flux, as well as its cellular function(s), remain to be elucidated. In this study, we demonstrate that MT-flux is sequentially driven from prometaphase to metaphase by CENP-E/kinesin-7 at KTs and KIF4A/kinesin-4 on chromosome arms, respectively, and these kinesins work in close cooperation with the MT-crosslinking motors EG5 and KIF15. We further propose that these activities are coordinated with the action of the MT-crosslinking molecules HSET and NuMA, which couple non-KT-MTs to KT-MTs, thereby ensuring a uniform distribution of spindle forces on metaphase KTs.

Lastly, we shed new light on the cellular function of MT-flux in human cells and propose a role in the regulation of mitotic spindle length by counteracting MCAK-mediated MT-depolymerizing activity on KT-MTs.

## Results

### KIF4A mediates MT-flux

In order to gain insight into the molecular mechanisms underlying MT-flux in human cells, we combined RNA interference (RNAi; Fig EV1) and chemical inhibitors with photoactivation-based spinning disk confocal live-cell imaging of late prometaphase/metaphase bipolar spindles and S-trityl-L-cysteine (STLC)-treated monopolar spindles in U2OS cells stably expressing photoactivatable (PA)-GFP tubulin (Fig 1A–C, Movies EV1 and EV2). We tested established contributors to MT-flux (kinesin-13/KIF2A, CLASP1 + 2 and kinesin-5/EG5), as well as several additional potential candidates (kinesin-12/KIF15, kinesin-7/CENP-E, kinesin-10/hKID, and kinesin-4/KIF4A). KIF2A was investigated because of its ability to depolymerize MT minus-ends at spindle poles and because of its previous implication in MT-flux (Ems-McClung & Walczak, 2010), whereas

CLASPs contribute to MT polymerization at the KT (Maiato et al, 2005; Maffini et al, 2009). hKID and KIF4A are chromokinesins, MT plus-end directed motor proteins localized on chromosome arms that generate chromosomal polar ejection forces (PEFs), promoting proper positioning of chromosome arms and accurate chromosome alignment and segregation (Rieder et al, 1986; Rieder & Salmon, 1994; Vernos et al, 1995; Antonio et al, 2000; Funabiki & Murray, 2000; Levesque & Compton, 2001; Mazumdar et al, 2004; Brouhard & Hunt, 2005; Wandke et al, 2012; Barisic et al, 2014; Tipton et al, 2017; Dong et al, 2018). KIF4A also interacts with PRC1 at interpolar MTs, facilitating accurate cytokinesis (Zhu & Jiang, 2005). CENP-E is a KT- and MT-localized plus-end directed motor protein required for congression of peripheral chromosomes and proper chromosome segregation (Yen et al, 1991; Schaar et al, 1997; Wood et al, 1997; Kapoor et al, 2006; Barisic et al, 2014). KIF15 is another plus-end directed motor with the ability to slide antiparallel MTs in a way similar to EG5 (Tanenbaum et al, 2009; Drechsler et al, 2014). Analysis of sum-projected kymographs (Fig 1D) excluded EG5, KIF15, and hKID as strong individual drivers of MT-flux (Fig 1E and F). However, depletion of KIF4A revealed a strong contribution to MT-flux, not only in bipolar spindles ( $0.32 \pm 0.14 \mu\text{m}/\text{min}$ , compared with  $0.61 \pm 0.22 \mu\text{m}/\text{min}$  in controls), as previously reported (Wandke et al, 2012), but also in monopolar spindles ( $0.33 \pm 0.11 \mu\text{m}/\text{min}$ , compared with  $0.5 \pm 0.14 \mu\text{m}/\text{min}$  in controls). Intriguingly, while inhibition of CENP-E did not significantly affect MT-flux in bipolar spindles ( $0.52 \pm 0.21 \mu\text{m}/\text{min}$ ; see also (Logarinho et al, 2012)), we detected a significant reduction of MT-flux in monopolar spindles ( $0.34 \pm 0.07 \mu\text{m}/\text{min}$ ; Fig 1E and F). As expected, depletion of KIF2A and CLASPs led to a strong reduction in flux rates in bipolar ( $0.17 \pm 0.12 \mu\text{m}/\text{min}$  and  $0.27 \pm 0.18 \mu\text{m}/\text{min}$ , respectively (see also (Maffini et al, 2009))) and monopolar spindles ( $0.17 \pm 0.09 \mu\text{m}/\text{min}$  and  $0.28 \pm 0.07 \mu\text{m}/\text{min}$ , respectively; Fig 1E and F), consistent with their respective roles in MT minus-end depolymerization and plus-end polymerization. These data are consistent with either of the proposed models of flux; however, in one model, KIF2A and CLASPs are interpreted as flux drivers, whereas in the other these are interpreted as part of cell's response to flux to regulate spindle length.

### KIF4A drives MT-flux via its chromosome arm-based motor activity

Because of its strong contribution, we sought to characterize the molecular mechanisms by which the chromokinesin KIF4A drives

**Figure 1. KIF4A mediates MT-flux.**

- A Representative spinning disk confocal live-cell imaging time series of U2OS cells stably co-expressing PA-GFP- $\alpha$ -tubulin (cyan) and mCherry- $\alpha$ -tubulin (red), treated with control and KIF4A siRNAs. White arrowheads highlight poleward motion of the photoactivated regions due to MT-flux. Scale bars, 10  $\mu\text{m}$ . Time, min:s.
- B Representative spinning disk confocal live-cell imaging time series images of S-trityl-L-cysteine (STLC)-treated U2OS cells stably co-expressing PA-GFP- $\alpha$ -tubulin (cyan) and mCherry- $\alpha$ -tubulin (red). Note that MT-flux is abrogated in the presence of taxol (lower panel). Scale bars, 10  $\mu\text{m}$ . Time, min:s.
- C Illustration of 405 nm laser-photoactivated regions in monopolar spindles (blue circles, left). The effect of photoactivation and region selected for kymograph generation (dashed white rectangle, right). Scale bar, 10  $\mu\text{m}$ .
- D Corresponding kymograph profiles of the photoactivated regions in bipolar and monopolar spindles used for quantification of the flux rates (red dotted lines highlight MT-flux slopes). Scale bars, 30 s.
- E, F Quantification of MT-flux in bipolar (E) and monopolar (F) spindles subjected to indicated treatments. Graphs represent MT-flux of individual cells with mean  $\pm$  SD. *N* (number of cells, number of independent experiments): – bipolar spindles: siControl (49, 5), STLC (31, 3), siKIF15 (39, 3), siKID (32, 3), siKIF4A (28, 3), siKIF2A (36, 3), siCLASPs (21, 2), GSK923295 (44, 3); – monopolar spindles: siControl (35, 3), siKIF15 (44, 3), siKID (38, 3), siKIF4A (44, 3), siKIF2A (38, 3), siCLASPs (12, 2), GSK923295 (33, 3). *P*-values were calculated against control using one-way ANOVA and Kruskal–Wallis *H*-test. n.s.—not significant, \*\*\*\**P*  $\leq$  0.0001.

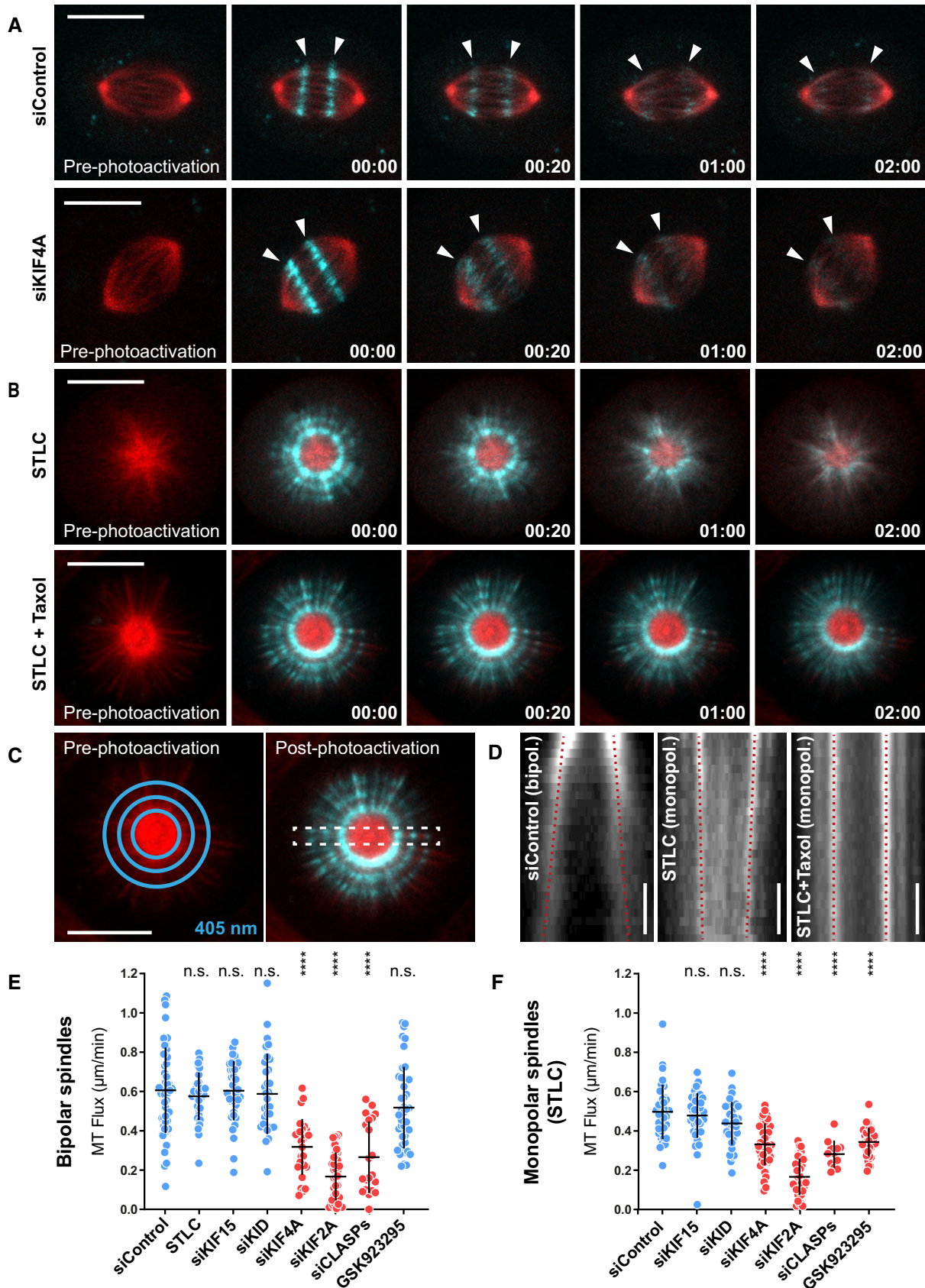


Figure 1.

MT-flux. First, we examined the effect of KIF4A overexpression on MT-flux rates. To do so, we designed a dose-response system by cloning KIF4A into an adenoviral vector to infect target cells with increasing virus titers (multiplicity of infection ratios [MOI]; Fig EV2A). KIF4A overexpression resulted in increased MT-flux rates (Fig EV2B), supporting the hypothesis that KIF4A drives MT-flux. Although RNAi and overexpression experiments clearly showed the importance of KIF4A for MT-flux, it remained unclear how KIF4A contributed to this process. To address this question, we conditionally reconstituted KIF4A-depleted cells expressing near physiological levels of RNAi-resistant versions of wild-type KIF4A, the ATPase-dead K94A motor mutant, and a chromatin non-binding KIF4A mutant ( $\Delta$ Zip1) that was still able to bind to central spindle inter-polar MTs (Wu & Chen, 2008; Sigl *et al*, 2014) (Figs 2A and B, and EV2C and Movie EV3). While wild-type KIF4A successfully rescued the reduced MT-flux rates in KIF4A RNAi cells ( $0.53 \pm 0.15 \mu\text{m}/\text{min}$ , compared with  $0.57 \pm 0.1 \mu\text{m}/\text{min}$  in uninduced cells and to  $0.29 \pm 0.13 \mu\text{m}/\text{min}$  in KIF4A shRNA), neither the motor mutant (K94A;  $0.32 \pm 0.14 \mu\text{m}/\text{min}$ , compared with  $0.61 \pm 0.15 \mu\text{m}/\text{min}$  in uninduced cells), nor the chromatin-binding mutant ( $\Delta$ Zip1;  $0.3 \pm 0.1 \mu\text{m}/\text{min}$ , compared with  $0.63 \pm 0.13 \mu\text{m}/\text{min}$  in uninduced cells) were able to recover MT-flux rates (Fig 2A and C). These results indicate that both the motor activity and localization of KIF4A on chromosome arms are essential for MT-flux (Fig 2D).

Based on these data, we speculate that after helping chromosomes to congress to the metaphase plate during early mitosis (Wandke *et al*, 2012), KIF4A cannot push the chromosomes any further due to equivalent forces applied from opposite spindle sides. Nevertheless, processive KIF4A on interacting MTs would provide the reactive force necessary to drive poleward flux (Fig EV2D).

To further elucidate the involvement of chromatin in MT-flux, we established U2OS cells to undergo mitosis with unreplicated genomes (MUGs) (Brinkley *et al*, 1988; O'Connell *et al*, 2008), in which chromatin is physically detached from spindle MTs (Figs 3A and C, and EV4B, and Movie EV4). In agreement with the data obtained using KIF4A mutants, MT-flux in bipolar MUG spindles was strongly reduced ( $0.31 \pm 0.13 \mu\text{m}/\text{min}$ , compared with  $0.5 \pm 0.13 \mu\text{m}/\text{min}$  in control cells treated with caffeine alone; Fig 3B), consistent with the importance of chromatin as the locus of KIF4A activity relevant for MT-flux. However, other features that are normally present in MUGs, such as merotelic KT-MT attachments, cannot be excluded to contribute to the observed attenuation of MT-flux.

### The MT-crosslinking proteins HSET and NuMA facilitate the distribution of MT-flux associated spindle forces on metaphase chromosomes

If our model based on KIF4A driving MT-flux from chromosome arms was correct, one would predict that the action of MT crosslinking molecules is required to transmit spindle forces from fluxing non-KT-MTs to KT-MTs, as proposed by the “coupled spindle” model (Matos *et al*, 2009). In order to test this hypothesis, we investigated the contribution of three well-established MT-crosslinking proteins to MT-flux, namely NuMA, kinesin-14/HSET, and PRC1. NuMA localizes to the spindle poles together with the MT minus-end-directed motor Dynein to crosslink and focus MT minus-ends (Merdes *et al*, 1996; Radulescu & Cleveland, 2010; Hueschen *et al*, 2017). HSET is a MT minus-end-directed kinesin motor with the ability to crosslink and slide antiparallel MTs, thereby generating an inward force within the spindle, similar to that proposed for Dynein (Mountain *et al*, 1999). PRC1 is involved in the assembly of the central spindle during late mitosis (Mollinari *et al*, 2002) and acts as a crosslinker between KT-MTs and bridging inter-polar MTs throughout mitosis (Kajtez *et al*, 2016; Polak *et al*, 2017; Vukusic *et al*, 2017; Suresh *et al*, 2020). We found that, while depletion of NuMA and/or HSET significantly reduced MT-flux rates ( $0.48 \pm 0.13$ ,  $0.36 \pm 0.13$ , and  $0.35 \pm 0.16 \mu\text{m}/\text{min}$ , respectively; Figs 4A and B, and EV3A, and Movie EV5), depletion of PRC1 had no such effect ( $0.61 \pm 0.22 \mu\text{m}/\text{min}$ , compared with  $0.61 \pm 0.22 \mu\text{m}/\text{min}$  in control cells; Figs 4B and EV3A). Thus, KIF4A's requirement for MT-flux is independent of its PRC1-dependent localization at inter-polar MTs (Kurasawa *et al*, 2004; Nguyen *et al*, 2018), further strengthening the argument of its association with chromatin in driving MT-flux.

In order to dissect whether the contribution of HSET for MT-flux depends on its MT-crosslinking ability, or on its motor activity, we designed a rescue experiment in which we individually expressed WT HSET and a non-processive motor mutant that is still able to crosslink MTs (N593K) (Cai *et al*, 2009b). Because our HSET constructs were GFP-tagged and could thus interfere with the PA-GFP tubulin signal, we used a U2OS cell line stably expressing green-red photoconvertible mEOS-tubulin (Wandke *et al*, 2012) (Fig EV3B). By monitoring MT-flux rates after depletion of endogenous HSET by 3'UTR-targeting siRNAs ( $0.37 \pm 0.13 \mu\text{m}/\text{min}$ , compared with  $0.61 \pm 0.13 \mu\text{m}/\text{min}$  in control cells), we observed that both WT HSET and the motor mutant successfully ensured normal MT-flux ( $0.59 \pm 0.1 \mu\text{m}/\text{min}$  and  $0.55 \pm 0.11 \mu\text{m}/\text{min}$ ,

#### Figure 2. KIF4A drives MT-flux via its chromosome arm-based motor activity.

- A Representative spinning disk confocal live-cell imaging time series images of U2OS PA-GFP- $\alpha$ -tubulin cells conditionally co-expressing KIF4A shRNA and RNAi-resistant mCherry-Kif4A variants induced using doxycycline. Chromosomes were stained using SiR-DNA. White arrowheads highlight poleward flux of the photoactivated regions. Scale bar, 10  $\mu\text{m}$ . Time, min:s.
- B Representative immunoblot of cell lysates obtained before and after doxycycline induction to validate the efficiency of KIF4A shRNA construct and expression of the RNAi-resistant mCherry-KIF4A variants. The anti-KIF4A antibody was used, together with anti-vinculin antibody as a loading control.
- C Quantification of MT-flux upon shRNA-mediated depletion of KIF4A alone or in combination with conditional expression of the RNAi-resistant mCherry-KIF4A variants. The bars in graph represent mean  $\pm$  SD. *N* (number of cells, number of independent experiments): uninduced shKIF4A (48, 4), shKIF4A (60, 4), uninduced KIF4A WT (36, 5), shKIF4A + KIF4A WT (43, 5), uninduced KIF4A K94A (42, 7), shKIF4A + KIF4A K94A (38, 6), uninduced KIF4A  $\Delta$ Zip1 (32, 4), and shKIF4A +  $\Delta$ Zip1 (30, 4). *P*-values were calculated using Student's *t*-test and Mann-Whitney *U*-test. n.s.—not significant, \*\*\*\**P*  $\leq$  0.0001.
- D Model illustrating chromosome arms-localized KIF4A driving MT-flux.



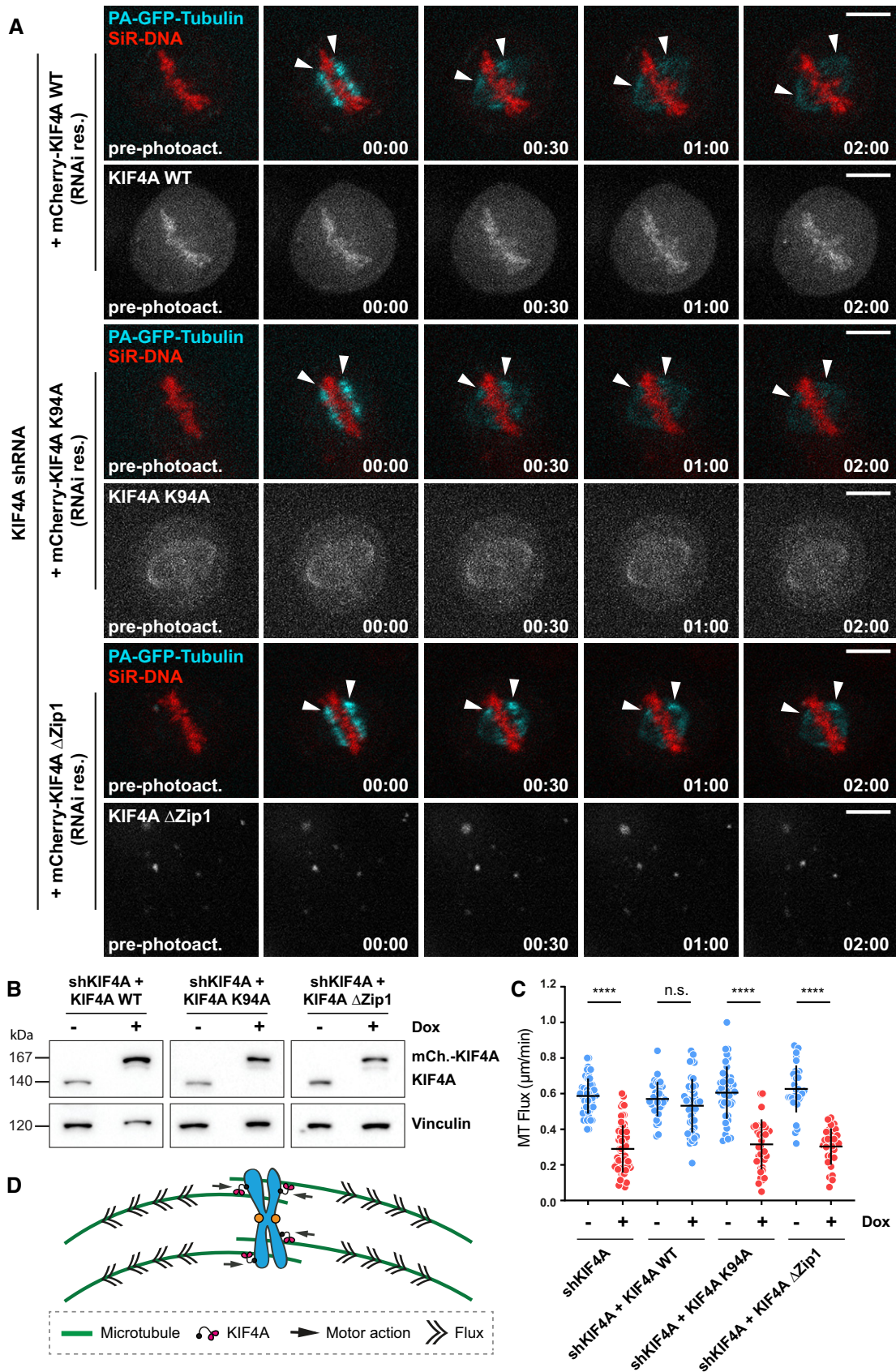
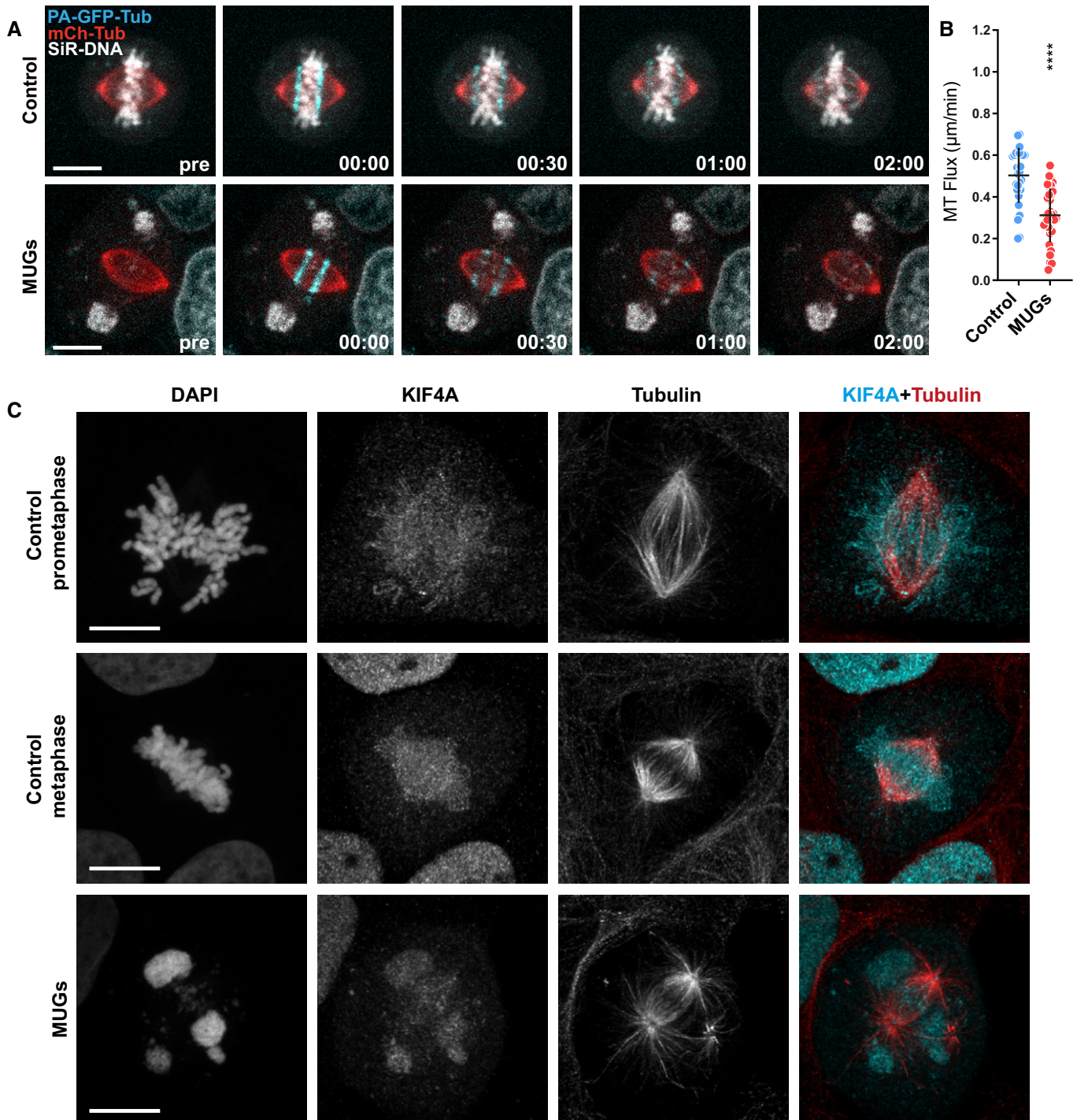


Figure 2.





**Figure 3. Bipolar spindles with expelled chromatin in MUGs exhibit reduced MT-flux.**

**A** Representative spinning disk confocal time series of MT-flux in bipolar spindles in control cells and cells undergoing mitosis with unreplicated genomes (MUGs). U2OS cells stably co-expressing PA-GFP- $\alpha$ -tubulin (cyan) and mCherry- $\alpha$ -tubulin (red), labeled for chromosomes with SiR-DNA (gray) are shown, with 5 mM caffeine used as a control. Scale bar, 10  $\mu\text{m}$ . Time, min:s.

**B** Quantification of the MT-flux rates from indicated conditions. MT-flux values with mean  $\pm$  SD are plotted. *N* (number of cells, number of independent experiments): Caffeine-only control (30, 3) and MUGs (34, 3). *P*-values from Mann–Whitney *U*-test. \*\*\*\**P*  $\leq$  0.0001.

**C** Representative point-scanning confocal maximum-intensity projected images of mitotic spindles in U2OS cells subjected to indicated conditions, immunostained with antibodies against KIF4A and  $\alpha$ -tubulin. DNA was counterstained with DAPI. KIF4A in cyan and  $\alpha$ -tubulin in red in merged image. Scale bar, 10  $\mu\text{m}$ .

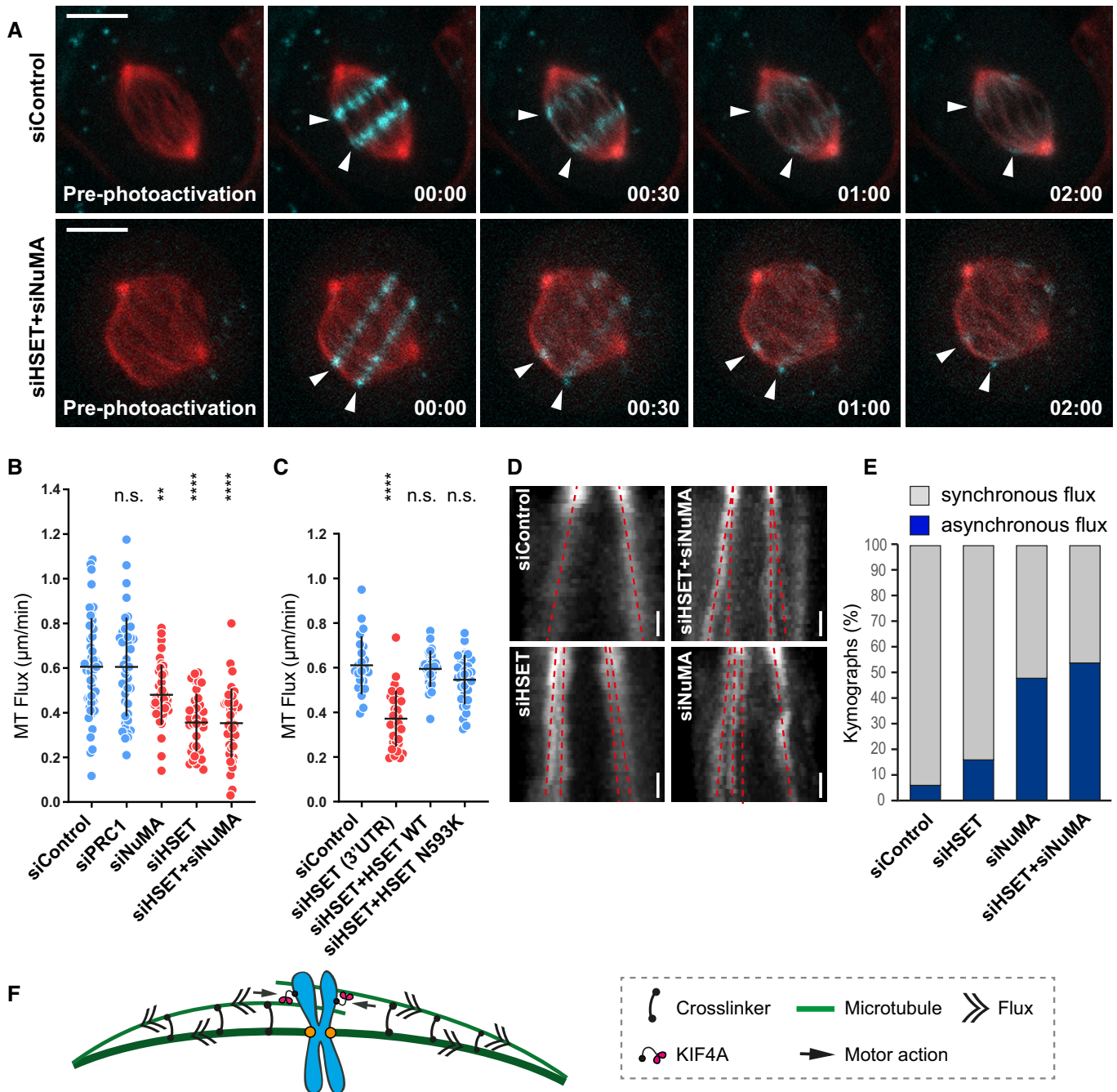


**Figure 4. The MT-crosslinking proteins HSET and NuMA facilitate the distribution of MT-flux associated spindle forces on metaphase chromosomes.**

- A** Representative spinning disk confocal live-cell image series of MT-flux in U2OS cells stably co-expressing PA-GFP- $\alpha$ -tubulin (cyan) and mCherry- $\alpha$ -tubulin (red) treated with indicated siRNAs. White arrowheads highlight poleward motion of the photoactivated regions due to MT-flux. Scale bars, 10  $\mu$ m. Time, mins.
- B** Quantification of the impact of the MT-crosslinking proteins on MT-flux in U2OS PA-GFP/mCherry- $\alpha$ -tubulin cells transfected with respective siRNAs. Graph represent MT-flux values with mean  $\pm$  SD. *N* (number of cells, number of independent experiments): siControl (49, 5), siPRC1 (45, 3), siNuMA (40, 3), siHSET (37, 3), and siHSET + siNuMA (39, 3). *P*-values were calculated against control using one-way ANOVA. n.s., not significant, \*\**P*  $\leq$  0.01, \*\*\*\**P*  $\leq$  0.0001.
- C** Quantification of the impact of the motor activity of HSET on MT-flux in U2OS cells stably expressing mEOS- $\alpha$ -tubulin treated with control or HSET 3'UTR siRNAs in presence or absence of the respective RNAi-resistant GFP-HSET constructs. Graph represent MT-flux values with mean  $\pm$  SD. *N* (number of cells, number of independent experiments): siControl (23, 3), siHSET 3'UTR (33, 3), siHSET 3'UTR + HSET WT (29, 5), and siHSET 3'UTR + HSET N593K (30, 4). *P*-values were calculated against control using one-way ANOVA. n.s., not significant, \*\*\*\**P*  $\leq$  0.0001.
- D** Representative kymographs of the photoactivated spindles from (B) displaying asynchronous flux motion (split of the two red dashed lines toward individual poles) upon RNAi-mediated depletion of MT-crosslinkers. Scale bars, 30 s.
- E** Percentage of cells with asynchronous flux movements calculated from (B).
- F** Model illustrating the role of MT-crosslinking activities of NuMA and HSET in uniform distribution of poleward forces across the mitotic spindle.



respectively; Figs 4C and EV3C). This suggests that MT-flux relies on HSET MT-crosslinking capacity, rather than its motor activity (Fig 4F). Interestingly, spindles depleted of NuMA and HSET revealed a frequent occurrence of asynchronous flux tracks, as inferred from a multi-stripe pattern on the kymographs of

photoactivated spindles (6% in control cells, 16% in HSET RNAi, 48% in NuMA RNAi, and 54% in HSET + NuMA RNAi; Fig 4D and E), suggesting weakened mechanical coupling between non-KT-MTs and KT-MTs. Altogether, these data suggest that MT-crosslinking activities of NuMA and kinesin-14/HSET are required to transmit

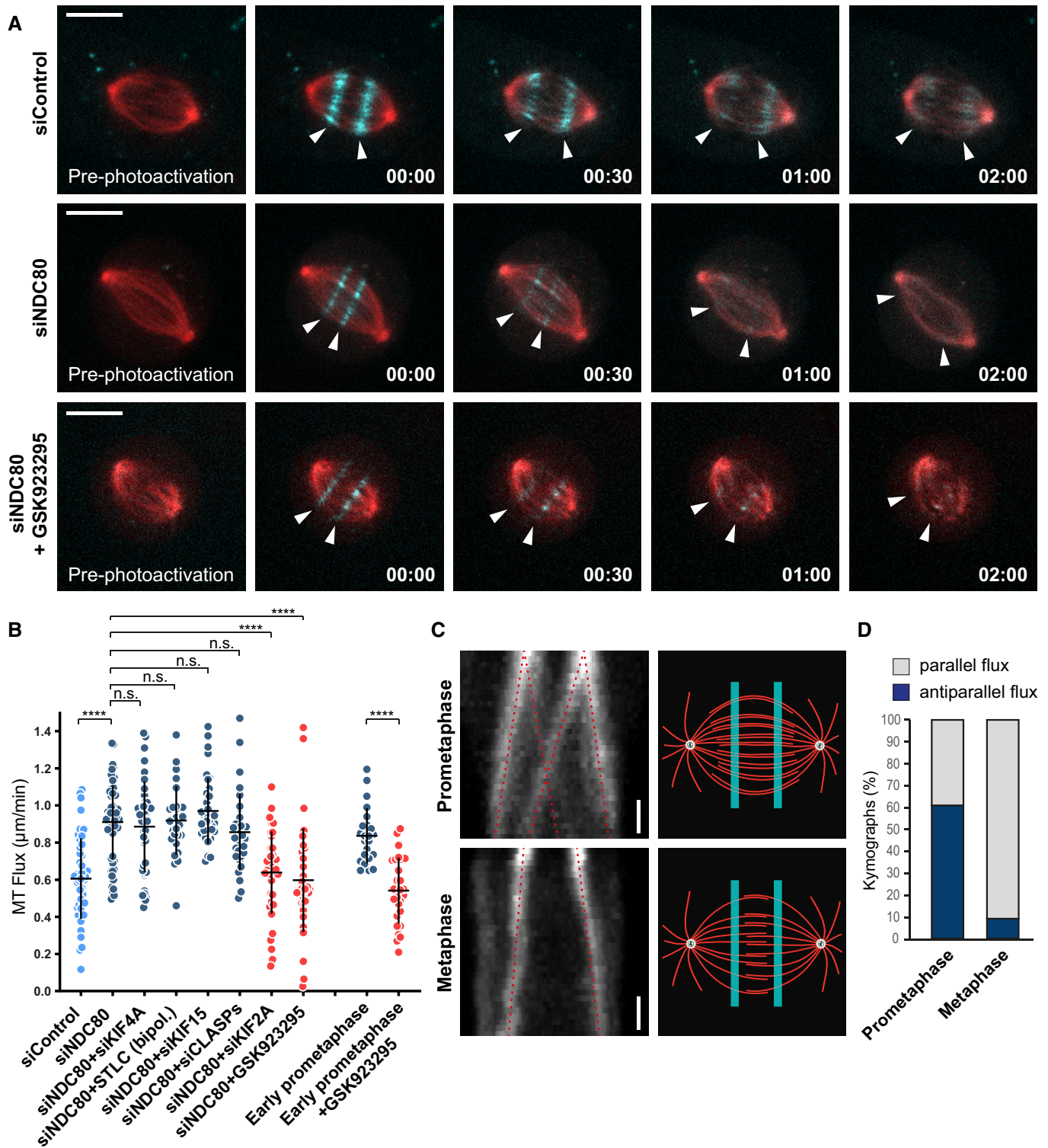


Figure 5.



**Figure 5. CENP-E is the predominant driver of MT-flux in early prometaphase.**

- A Representative spinning disk confocal live-cell time series of MT-flux in U2OS cells stably co-expressing PA-GFP- $\alpha$ -tubulin (cyan) and mCherry- $\alpha$ -tubulin (red) treated with indicated conditions. White arrowheads follow the poleward motion of the photoactivated regions due to MT-flux. Scale bars, 10  $\mu$ m. Time, mins.
- B Quantification of the impact of stable end-on KT-MT attachments on MT-flux in NDC80-depleted cells under indicated conditions and in early prometaphase cells with and without the CENP-E inhibitor GSK923295. MT-flux values are plotted with mean  $\pm$  SD. *N* (number of cells, number of independent experiments): siControl (49, 5), siNDC80 (59, 6), siNDC80 + siKIF4A (41, 3), siNDC80 + STLC (bipol.) (28, 3), siNDC80 + siKIF15 (36, 4), siNDC80 + siCLASPs (33, 3), siNDC80 + siKIF2A (38, 4), siNDC80 + GSK923295 (38, 3), early prometaphase (23, 3), and early prometaphase + GSK923295 (28, 3). *P*-values were calculated using Kruskal–Wallis *H*-test compared with siNDC80, except for early prometaphase data for which Student's *t*-test was used. n.s., not significant, \*\*\*\**P*  $\leq$  0.0001.
- C Kymograph profiles (left) highlighting that the photoactivated regions in prometaphase (upper panel) split and move toward both poles, whereas metaphase spindles (lower panel) flux uniformly toward individual poles (indicated by red dotted lines). Illustration of the photoactivated regions (right) in prometaphase and metaphase spindles, highlighting that interpolar MTs overlap over a broader region in early mitosis, becoming focused at the spindle equator in metaphase. Scale bar, 30 s.
- D Percentage of cells with parallel and antiparallel flux movements during prometaphase and metaphase. *N* (number of cells, number of independent experiments): prometaphase (23, 3), metaphase (22, 3).

the MT-flux forces generated on non-KT-MTs to KT-MTs, thereby promoting a uniform distribution of spindle forces on metaphase chromosomes (Fig 4F).

### CENP-E is the predominant driver of MT-flux in early prometaphase

Another prediction of the “coupled spindle” model is that KT-MTs flux at slightly slower rates compared with non-KT-MTs due to imperfect coupling (Matos *et al*, 2009). Indeed, this was shown to be the case in insect spermatocytes (LaFountain *et al*, 2004), *Xenopus* oocyte spindles assembled *in vitro* (Maddox *et al*, 2003) and human cells (Lecland & Luders, 2014). To examine this further in human cells, we measured MT-flux rates after perturbation of end-on KT-MT attachments by depletion of NDC80/HEC1, the main MT-anchoring protein at KTs (Wigge & Kilmartin, 2001; DeLuca *et al*, 2002; McClelland *et al*, 2003; Cheeseman *et al*, 2006; Wei *et al*, 2007) (Fig EV4A). Indeed, MTs in these cells fluxed faster ( $0.91 \pm 0.2 \mu\text{m}/\text{min}$ ; Fig 5A and B, and Movie EV6), suggesting that stable end-on KT-MT attachments work as flux brakes, in agreement with the “coupled spindle” model. Remarkably, depletion of KIF4A did not compromise MT-flux after NDC80 RNAi (Figs 5B and EV4A), suggesting that KIF4A is dispensable for MT-flux prior to the establishment of end-on KT-MT attachments (Figs 4F and EV2D).

To investigate the molecular mechanism underlying MT-flux before the establishment of stable end-on KT-MT attachments, we further examined the potential contributions of EG5 and KIF15 (Figs 5B and EV4A). Similar to the effect of KIF4A depletion, neither EG5 inhibition nor depletion of KIF15 reduced MT-flux rate after NDC80 RNAi. Since CENP-E inhibition had a negative impact on MT-flux rate exclusively in monopolar spindles, which contain less end-on KT-MT attachments (Kapoor *et al*, 2000; Shrestha & Draviam, 2013) (Fig 1E and F), we sought to inhibit CENP-E in NDC80-depleted cells. Unlike its knockdown, chemical inhibition of CENP-E keeps the inactive motor at KTs, allowing its interaction with CLASPs, thus excluding any potential indirect effects (Maffini *et al*, 2009; Logarinho *et al*, 2012). Strikingly, CENP-E inhibition in NDC80-depleted cells strongly decreased MT-flux rate ( $0.6 \pm 0.28 \mu\text{m}/\text{min}$ , compared with  $0.91 \pm 0.2 \mu\text{m}/\text{min}$  in NDC80 RNAi; Fig 5A and B, and Movie EV6), similar to the effect of NDC80 co-depletion with KIF2A ( $0.64 \pm 0.22 \mu\text{m}/\text{min}$ ; Figs 5B and EV4A). Importantly, co-depletion of NDC80 and CLASPs did not reduce MT-flux rate ( $0.86 \pm 0.21 \mu\text{m}/\text{min}$ ) compared with NDC80 knockdown (Figs 5B and EV3A), in agreement with the recently proposed role of CLASPs in sustaining the growth of KT-attached MTs

necessary for flux (Girao *et al*, 2020), and further demonstrating the specificity of the observed CENP-E phenotype.

Taken together, these data suggest that CENP-E drives MT-flux in early prometaphase, prior to the establishment of stable end-on KT-MT attachments. To directly test this, we first compared flux rates between early and late prometaphase/metaphase and found that MT-flux in early prometaphase was indeed faster ( $0.84 \pm 0.15$  and  $0.61 \pm 0.22 \mu\text{m}/\text{min}$ , respectively; Figs 5B and EV5A), consistent with the increased flux found in NDC80-depleted cells. Subsequent measurement of MT-flux in CENP-E-inhibited early prometaphase cells showed a significant decrease in MT-flux rate ( $0.54 \pm 0.18 \mu\text{m}/\text{min}$ ; Fig 5B), comparable to the one observed upon CENP-E inhibition in NDC80-depleted cells. We concluded that CENP-E motor activity is required for MT-flux prior to the establishment of end-on KT-MT attachments, independently from its role in CLASPs recruitment to KTs.

Unlike in metaphase, photoactivated tubulin marks in early prometaphase showed splitting and moved simultaneously toward both poles (61% in prometaphase, compared with 9% in metaphase; Figs 5C and D, and EV5A, and Movie EV7), as it was observed in *in vitro*-assembled *Xenopus* egg extract spindles (Sawin & Mitchison, 1991). This strongly suggests that interpolar MTs overlap over a broader region in early mitosis, but then become more restricted to the spindle equator as cells reach metaphase. The broad distribution of antiparallel MTs in early mitosis coincides with CENP-E localization at laterally attached KTs during “prometaphase rosette” configuration (Itoh *et al*, 2018) (Figs 6A and B, and EV4B), and is consistent with the localization of the antiparallel MT-crosslinker PRC1, which also covers a wider region in prometaphase (Fig EV5B). To gain a deeper mechanistic insight into how CENP-E drives MT-flux in early mitosis, we used super-resolution coherent-hybrid STED (CH-STED) microscopy (Pereira *et al*, 2019) to more accurately determine CENP-E localization in the complex context of the mitotic spindle (Fig 6A and B). Surprisingly, apart from its well-established localization at KTs (Figs 6A and B, and EV4B) (Yen *et al*, 1991; Schaar *et al*, 1997; Wood *et al*, 1997; Kapoor *et al*, 2006) and antiparallel midzone MTs during late anaphase and telophase (Yen *et al*, 1991), we found that CENP-E also localized at interpolar MTs, both in control and NDC80-depleted early mitotic cells (Fig 6A and B). These observations raised two possible explanations for how CENP-E could drive MT-flux prior to the establishment of end-on KT-MT attachments. On one hand, given CENP-E's localization at the expanded fibrous corona of unattached outer KTs during early mitosis (Figs 6A and B, and EV4B), and its lateral association with spindle MT bundles in the absence of K-fibers (Cai *et al*, 2009a), KT-localized

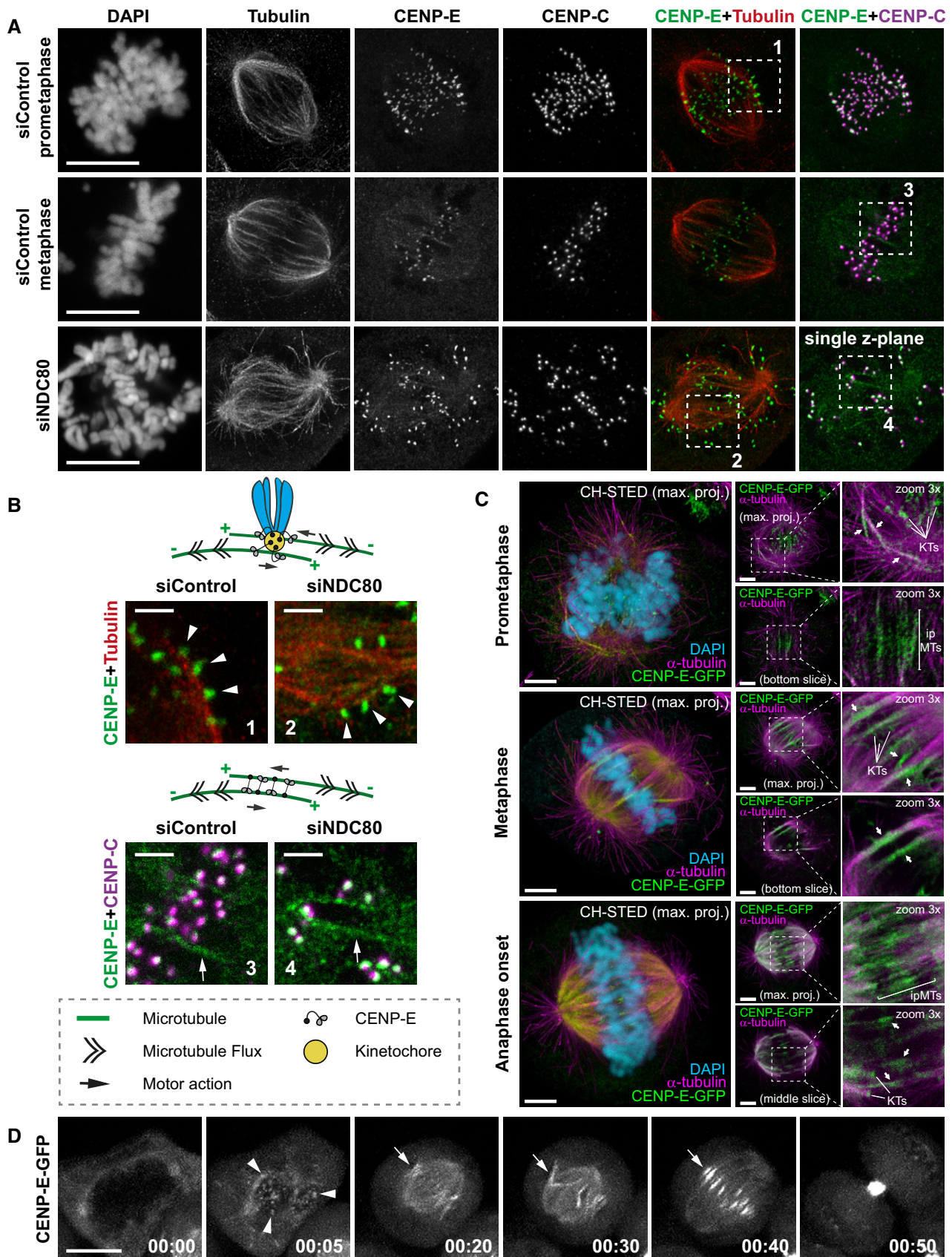


Figure 6.

**Figure 6. CENP-E localizes to KTs and MT bundles, including overlapping antiparallel MTs during early mitosis.**

- A Representative maximum-intensity projected coherent-hybrid STED (CH-STED) images of mitotic spindles in U2OS cells treated with control and NDC80 siRNAs and stained for DNA (DAPI), KTs (CENP-C, magenta),  $\alpha$ -tubulin (red), and CENP-E (green). Scale bar, 10  $\mu$ m.
- B Model illustrating potential mechanisms for CENP-E mediated MT-flux forces either through its KT- or antiparallel MT-based localization and sliding. Zoomed insets from (A) highlight CENP-E localized at KTs laterally interacting with MTs (white arrowheads in 1, 2), and CENP-E localized at interpolar MTs (white arrows in 3, 4), in control and NDC80-depleted mitotic cells. Scale bars, 2  $\mu$ m.
- C CH-STED analyses of HeLa cells stably expressing CENP-E-GFP illustrating bipolar spindles in prometaphase, metaphase and just after sister-chromatid separation at anaphase onset. Approximate  $x$ - $y$  resolution is 70 nm. The expected/described localization of CENP-E-GFP (green) at KTs is shown. In addition, CENP-E-GFP was found associated with interpolar MTs (ipMTs), including regions of overlapping antiparallel MTs, and k-fibers. Chromosomes (confocal mode only) were revealed in the larger panels with DAPI (cyan) and MTs (magenta) were detected with an anti- $\alpha$ -tubulin antibody. Arrows indicate examples of clear MT bundles, including regions of overlapping antiparallel MTs. Scale bar in all panels is 5  $\mu$ m.
- D Representative spinning disk confocal live-cell time series of HeLa cells stably expressing CENP-E-GFP. White arrowheads highlight CENP-E-GFP at KTs, white arrows highlight CENP-E-GFP on interpolar MTs. Scale bar, 10  $\mu$ m. Time, h:min.

CENP-E might interact with antiparallel interpolar MTs, sliding them apart toward the poles (Fig 6B). This would be consistent with a role for CENP-E in the transition from lateral to end-on KT-MT attachments (Shrestha & Draviam, 2013; Sikirzhyski *et al*, 2018; Chakraborty *et al*, 2019). On the other hand, CENP-E might directly crosslink antiparallel MTs and slide them apart (Fig 6B). To further investigate this novel CENP-E localization on interpolar MTs in early mitosis, we used HeLa cells stably expressing a bacterial artificial chromosome encoding CENP-E-GFP under control of its own promoter (Poser *et al*, 2008) (Fig 6C and D, and Movie EV8). Both CH-STED imaging (Fig 6C) and spinning disk confocal live-cell imaging (Fig 6D and Movie EV8) confirmed the presence of CENP-E on interpolar MTs throughout mitosis. Noteworthy, CH-STED imaging clearly showed that CENP-E exclusively colocalized with more stable spindle MTs and was excluded from astral MTs, in line with our earlier finding that CENP-E has a bias toward detyrosinated MTs (Barisic *et al*, 2015). Moreover, CENP-E-GFP was associated with non-KT-MT bundles, but not with individual astral MTs even in STLC-treated monopolar spindles, but whether these bundled MTs are parallel or antiparallel could not be determined (Fig EV4C). Thus, CENP-E localizes to both KTs and non-KT-MT bundles (including antiparallel MTs) throughout mitosis in human cells.

Since earlier work showed that CENP-E localization at the spindle midzone in late anaphase depends on PRC1 (Kurasawa *et al*, 2004), we tested whether CENP-E localization on interpolar MTs in early mitosis also depended on PRC1. Depletion of PRC1 both in HeLa cells stably expressing CENP-E-GFP and in NDC80-depleted U2OS cells, led to a complete removal of CENP-E from interpolar MTs, but not from KTs, indicating that CENP-E association with interpolar MTs in early mitosis also depends on PRC1 (Figs EV6A and B). Next, we applied this knowledge to dissect which CENP-E pool (KTs vs. interpolar MTs) is more relevant for MT-flux in early mitosis. We used NDC80-depleted cells lacking stable end-on KT-MT attachments, as the condition where the contribution of CENP-E to MT-flux was most prominent (Fig 5A and B), to compare the respective impacts of PRC1 and CENP-E inactivation on MT-flux. Unlike CENP-E inhibition (Fig 5A and B), PRC1 depletion did not reduce MT-flux rate in NDC80-depleted cells ( $1.02 \pm 0.16 \mu\text{m}/\text{min}$ , compared with  $0.91 \pm 0.2 \mu\text{m}/\text{min}$  in NDC80 RNAi; Fig EV6C), suggesting that the observed role of CENP-E on MT-flux relies more on its KT-associated pool, rather than on its interpolar MT localization. In agreement, as the localization of CENP-E during mitosis gradually decreases at KTs and increases at the interpolar MTs, its impact on MT-flux simultaneously declines from prometaphase to metaphase.

**Combined action of EG5 and KIF15 support MT-flux driving activities of CENP-E and KIF4A**

Although we identified CENP-E and KIF4A as drivers of MT-flux in prometaphase and metaphase, respectively, functional inactivation of either of these two motors resulted in only around 50% decrease in MT-flux rate, indicating the presence of other important contributor(s). Therefore, we tested whether EG5 and KIF15 play a synergistic role in driving MT-flux. Importantly, in contrast to their individual functional inactivation, which did not affect MT-flux rates (Fig 1E), inhibition of EG5 in KIF15-depleted cells resulted in a significant decrease of MT-flux in bipolar spindles ( $0.43 \pm 0.11 \mu\text{m}/\text{min}$ , compared with  $0.61 \pm 0.22 \mu\text{m}/\text{min}$  in controls), as well as in NDC80-depleted spindles ( $0.52 \pm 0.13 \mu\text{m}/\text{min}$ , compared with  $0.91 \pm 0.2 \mu\text{m}/\text{min}$  in NDC80 RNAi only; Fig 7B and C), suggesting that these two antiparallel MT-sliding motors play redundant roles, similar to their role in bipolar spindle assembly (Tanenbaum *et al*, 2009). Therefore, we examined whether MT-flux is driven by the cooperative actions between CENP-E, EG5, and KIF15 prior to the establishment of stable end-on KT-MT attachments. Strikingly, triple inactivation of CENP-E, EG5, and KIF15 resulted in virtually no flux both in NDC80-depleted cells ( $0.1 \pm 0.09 \mu\text{m}/\text{min}$ , compared with  $0.91 \pm 0.2 \mu\text{m}/\text{min}$  in NDC80 RNAi only) and in early prometaphase cells ( $0.07 \pm 0.11 \mu\text{m}/\text{min}$ , compared with  $0.84 \pm 0.15 \mu\text{m}/\text{min}$  in control early prometaphase cells; Fig 7A and B, and Movie EV9). Next, we tested whether EG5 and KIF15 also cooperate with KIF4A to drive MT-flux upon the establishment of stable end-on KT-MT attachments. Triple inactivation of KIF4A, EG5 and KIF15 in late prometaphase/metaphase cells led to a much stronger reduction in MT-flux, compared with either KIF4A-depletion or co-inactivation of EG5 and KIF15 ( $0.15 \pm 0.12 \mu\text{m}/\text{min}$ , compared with  $0.43 \pm 0.1 \mu\text{m}/\text{min}$  in STLC + KIF15 RNAi and  $0.32 \pm 0.14$  in KIF4A RNAi; Fig 7C and D, and Movie EV9). Altogether, these data demonstrate that mitotic MT-flux in human cells is sequentially driven by the coordinated action of 4 kinesins.

**MT poleward flux regulates spindle length in response to MCAK-mediated depolymerization of KT-MTs**

Similar to what was observed upon CLASPs depletion (Maffini *et al*, 2009), we observed substantial reduction of spindle length under certain conditions that resulted in highly attenuated MT-flux rates (Fig 7A and D). To investigate the relationship between MT-flux and spindle length, we analyzed the correlation between altered



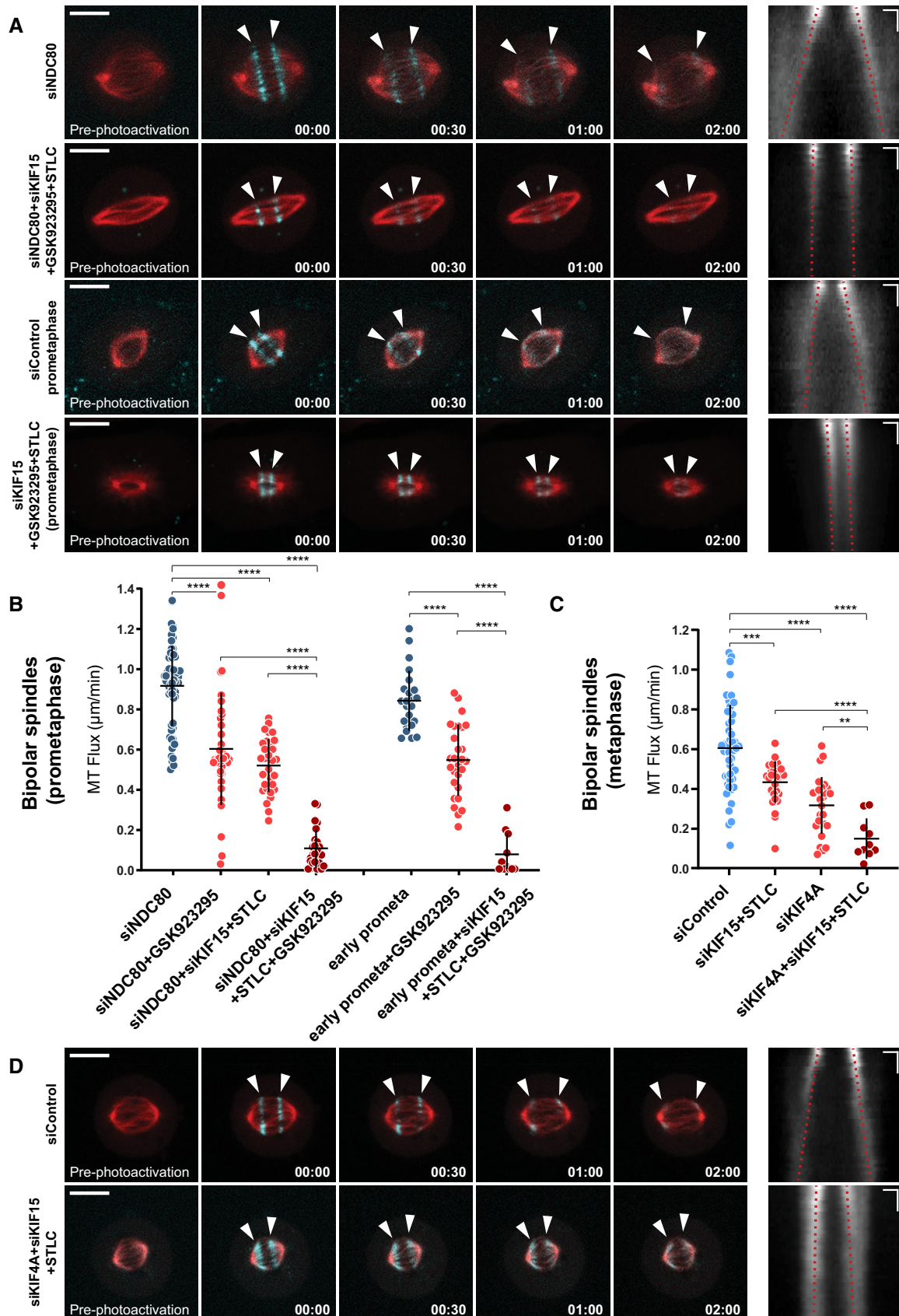


Figure 7.

**Figure 7. Combined action of EG5 and KIF15 support MT-flux driving activities of CENP-E and KIF4A.**

- A Representative spinning disk confocal time series of U2OS cells stably co-expressing PA-GFP- $\alpha$ -tubulin (cyan) and mCherry- $\alpha$ -tubulin (red), with indicated treatments (left). White arrowheads highlight poleward flux of the photoactivated regions. Scale bar, 10  $\mu$ m. Time, min:s. Right panels display corresponding kymographs of the photoactivated spindles used for quantification of the flux rates (red dotted lines highlight MT-flux slopes). Scale bars, 2  $\mu$ m (horizontal) and 30 s (vertical).
- B, C Quantification of MT-flux in prometaphase (B) and metaphase (C) bipolar spindles subjected to indicated treatments. Graphs represent MT-flux of individual cells with mean  $\pm$  SD. siNDC80, siNDC80 + GSK923295, early prometaphase, early prometaphase + GSK923295, siControl, and siKIF4A data are from Figs 1E and 5B. *N* (number of cells, number of independent experiments): siNDC80 + KIF15 + STLC (33, 5), siNDC80 + KIF15 + STLC + GSK923295 (25, 3), early prometaphase + KIF15 + STLC + GSK923295 (11, 2), siKIF15 + STLC (29, 3), siKIF4A + siKIF15 + STLC (10, 3). *P*-values were calculated using Student's *t*-test and Mann–Whitney *U*-test. \*\**P*  $\leq$  0.01, \*\*\**P*  $\leq$  0.001, \*\*\*\**P*  $\leq$  0.0001.
- D Representative spinning disk confocal time series of U2OS cells stably co-expressing PA-GFP- $\alpha$ -tubulin (cyan) and mCherry- $\alpha$ -tubulin (red), with indicated treatments (left) and corresponding kymographs (right) as described in (A). Scale bars, 2  $\mu$ m (horizontal) and 30 s (vertical).

MT-flux rates and spindle lengths from different treatments. We found that MT-flux rate and spindle length showed a strong positive correlation overall (Pearson correlation coefficient,  $r = 0.76$ ; *P* value =  $< 0.0001$ ; Fig 8A and Table EV1). Importantly, we noticed that spindle length did not dramatically change in NDC80-depleted cells with reduced flux rates, where no correlation between MT-flux rate and spindle length was observed (Pearson correlation coefficient,  $r = 0.69$ ; *P* value =  $0.1980$ ; Fig 8C). Accordingly, when we analyzed the correlation between MT-flux and spindle length in cells containing mainly stable end-on KT-MT attachments that displayed reduced flux, the correlation between MT-flux rate and spindle length was strong (Pearson correlation coefficient,  $r = 0.87$ ; *P* value =  $0.0119$ ; Fig 8B).

These data suggest that MT-flux regulates spindle length in response to the formation of stable end-on KT-MT attachments (Fig EV7A). Previously, it was shown that although depletion of MCAK (kinesin-13-family member with MT-depolymerizing activity (Desai *et al*, 1999)) alone did not affect MT-flux rate, its co-depletion with KIF2A not only strongly reduced MT-flux rate but also restored spindle bipolarity and size in KIF2A-depleted cells (Ganem & Compton, 2004; Ganem *et al*, 2005). Because simultaneous inactivation of KIF4A, EG5 and KIF15 in late prometaphase/metaphase cells led to much shorter spindles (Figs 7D, and 8A and B, Table EV1), we tested whether MT-flux regulates spindle length by preventing MCAK-mediated depolymerization of k-fibers. Strikingly, we found that spindle shortening after triple inactivation of KIF4A, EG5, and KIF15 was fully rescued upon co-depletion of MCAK ( $12.76 \pm 1.22 \mu\text{m}$  compared with  $9.5 \pm 1.49 \mu\text{m}$  in triple inactivated cells and  $13.3 \pm 1.79 \mu\text{m}$  in controls; Figs 8D and E, and EV7D). In addition to its effect on spindle length, MCAK co-depletion significantly reduced spindle collapsing in bipolar triple inactivated cells (Fig EV7B). To further investigate the impact of MCAK on spindle length in cells with reduced MT-flux, we co-depleted MCAK and CLASPs. Similar to its co-depletion in cells with triple inactivated KIF4A, EG5, and KIF15, depletion of MCAK also successfully recovered spindle length in CLASP-depleted cells (Fig 8E). Importantly, while MCAK depletion recovered spindle length in both of these conditions (Fig 8E), the MT-flux rates remained reduced (Fig EV7C). Finally, to dissect whether MT-flux regulates spindle length by counteracting specifically MCAK or kinesin-13-driven MT-depolymerizing activity in general, we co-depleted KIF2A in cells with triple inactivated KIF4A, EG5, and KIF15, as well as in CLASP-depleted cells. In contrast to co-depletion of MCAK, KIF2A co-depletion did not rescue spindle shortening neither after triple inactivation of KIF4A, EG5, and KIF15 nor in CLASP-depleted cells (Figs 8E and EV7D). Overall, these data

indicate that MT-flux regulates spindle length by specifically counteracting MCAK-driven MT-depolymerization on KT-MTs.

## Discussion

Mitotic spindle MTs remain highly dynamic even when the overall structure maintains a certain steady-state length. This is explained by the continuous poleward MT-flux, which is balanced by MT polymerization and depolymerization at their plus- and minus-ends, respectively. However, the drivers and functional role of MT poleward flux in human cells have remained elusive for more than three decades.

Our study establishes the long-sought molecular mechanisms underlying MT-flux and explains its role in regulating spindle length upon the establishment of stable end-on KT-MT attachments. Thus, MT-flux is not just an epiphenomenon of MT-dynamics but plays important roles for spindle function. Altogether, our findings support a model in which MT-flux in human cells is driven by the coordinated action of four kinesins. Accordingly, interpolar MTs are slid apart by the collaborative activity of the MT-sliding motors EG5 and KIF15, assisted by the sequential contribution of CENP-E at KTs in prometaphase and KIF4A on chromosome arms in metaphase (Fig 9). This sequential contribution of CENP-E and KIF4A might be explained by the fact that upon bi-orientation, a large amount of CENP-E is stripped away from the KTs (Howell *et al*, 2001) and therefore KIF4A gradually takes over during chromosome alignment to compensate for the weakened CENP-E contribution (Figs 4F and EV2D). In addition, we have previously shown that CENP-E is dominant over KIF4A in early mitosis (Barisic *et al*, 2014). In metaphase, KIF4A cannot move the chromosomes any further due to equivalent opposite forces, but instead, KIF4A might cause non-KT-MTs to flux toward the poles (Figs 9 and EV2D), contributing to MT-flux at this stage. Thus, because of its ability to move chromosomes away from the pole in prometaphase, KIF4A contributes to chromosome congression. However, when chromosomes align at the metaphase plate and cannot move further, KIF4A helps driving MT-flux.

Interestingly, although CENP-E inhibition prior to establishment of end-on KT-MT attachments, as well as KIF4A depletion in metaphase, strongly compromised MT-flux, the reduction was not complete (Figs 1E and 5B). This was explained by the fact that simultaneous abrogation of the functions of EG5 and KIF15, together with CENP-E inhibition in early mitosis, and KIF4A depletion in metaphase, respectively, resulted in virtually no flux (Fig 7A–D),

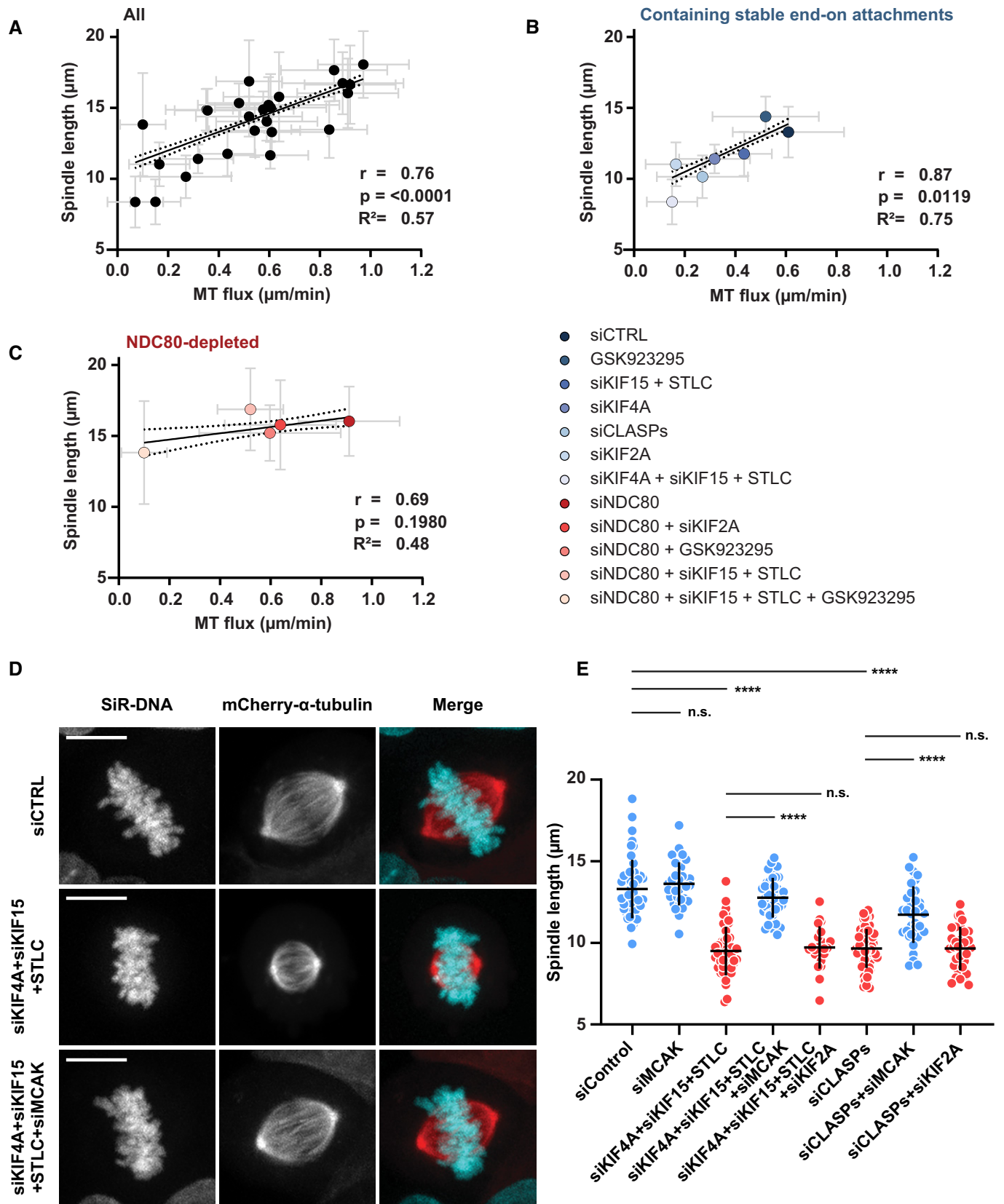


Figure 8.

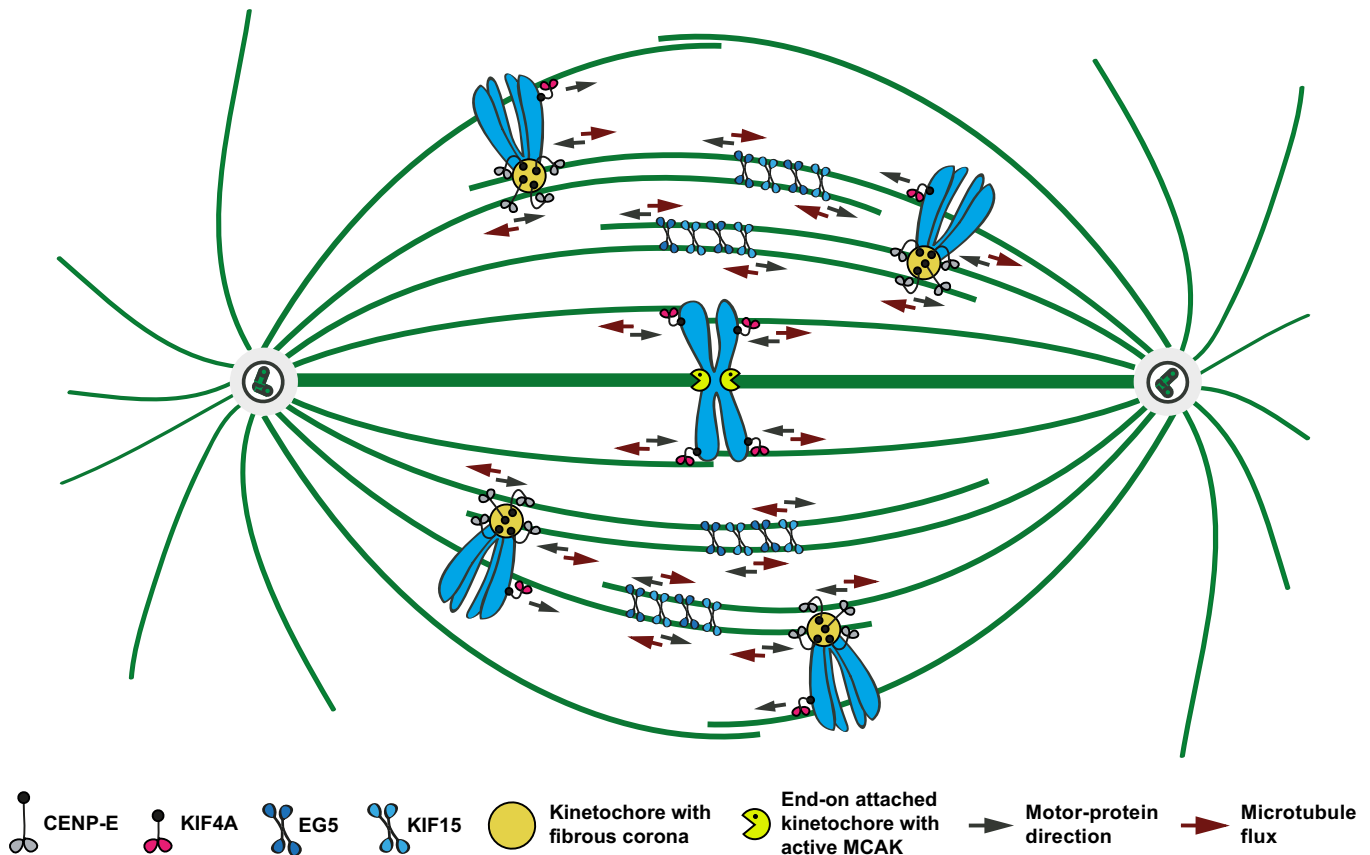


**Figure 8. MT poleward flux regulates spindle length in response to MCAK-mediated depolymerization of KT-MTs.**

A–C Graph depicting a direct correlation between MT-flux and mitotic spindle where mean spindle length is plotted over mean MT-flux rates for all indicated conditions (A), mitotic conditions containing stable end-on attachments (B), and NDC80 depleted conditions lacking stable end-on attachments (C). Solid and dotted lines represent the linear regression and 95% confidence interval, respectively. Pearson correlation coefficient ( $r$ ), coefficient of determination ( $r^2$ ), and corresponding  $P$ -values are indicated. The error bars over x and y axes represent the standard deviation of MT-flux and spindle length, respectively.

D Representative images from spinning disk confocal live-cell time series of U2OS PA-GFP- $\alpha$ -tubulin/mCherry- $\alpha$ -tubulin cells under indicated treatments, with SiR-DNA-labeled DNA. Microtubules are shown in red and DNA in cyan in the merged image. Scale bar: 10  $\mu$ m.

E Quantification of spindle lengths at metaphase following indicated treatments. Graph represents the spindle length of individual cells with mean  $\pm$  SD.  $N$  (number of cells, number of independent experiments): siControl (49, 5), siMCAK (34, 3), siKIF4A + siKIF15 + STLC (46, 6), siKIF4A + siKIF15 + STLC + siMCAK (43, 3), siKIF4A + siKIF15 + STLC + siKIF2A (22, 3), siCLASPs (64, 6), siCLASPs + siMCAK (33, 3), siCLASPs + siKIF2A (32, 3).  $P$ -values were calculated using Student's  $t$ -test and Mann–Whitney  $U$ -test. n.s.—not significant, \*\*\*\* $P \leq 0.0001$ .

**Figure 9. The model illustrating how MT poleward flux is driven by the coordinated action of four kinesins.**

In our MT-flux model, interpolar MTs are slid apart by the collaborative activity of the MT-crosslinking motors EG5 and KIF15, supported by sequential contribution of CENP-E at KTs in prometaphase and KIF4A on chromosome arms in metaphase. CENP-E at laterally attached KTs during early mitosis interacts with antiparallel MTs and slides them apart. During chromosome alignment to the metaphase plate, when CENP-E is partially stripped away from the KTs, KIF4A gradually takes over, promoting MTs to flux toward the poles.

demonstrating that MT-flux in human cells is driven by coordinated action of these four kinesins and further exposing the collaborative nature of the MT-flux-driving machinery.

During early mitosis, CDK1 and PLK1 phosphorylate PRC1, keeping it mostly inactive (Zhu *et al*, 2006; Hu *et al*, 2012). At anaphase onset, PRC1 is activated by dephosphorylation and brought to the midzone MTs by KIF4A (Zhu & Jiang, 2005). However, recent studies proposed PRC1 to bridge KT-MTs with interpolar MTs already during spindle assembly (Kajtez *et al*, 2016; Polak *et al*, 2017), opening the possibility that a pool of KIF4A co-localizes with PRC1 at interpolar MTs even before anaphase. Moreover, a recent study

showed that co-inactivation of KIF4A and EG5 in RPE-1 cells impaired the sliding of interpolar MTs during anaphase (preprint: Vukušić *et al*, 2019), thus suggesting that similar players are involved in MT-flux and MT-sliding in anaphase. Nevertheless, our KIF4A mutants- and PRC1 RNAi-based data suggest that the contribution of KIF4A to MT-flux depends on its motor activity and its localization on chromosome arms (Fig 2A and C), but not on its association with spindle midzone MTs (Figs 2A and C, and 4B). Thus, it will be of interest in future studies to address on which level the molecular basis of MT-flux and anaphase MT-sliding overlap.

Since KIF4A is not localized at KTs, the MT-fluxing force generated on chromosome arms has to be transmitted to KT-MTs. We showed that MTs fluxed faster in NDC80-depleted cells, indicating that stable KT-MT end-on attachments normally work as flux brakes (Fig 5A and B). This is in line with earlier observations in *Xenopus* egg extracts (Maddox *et al*, 2003), crane-fly spermatocytes (LaFountain *et al*, 2004), and human cells (Lecland & Luders, 2014) that, likely due to a drag, KT-MTs flux slightly slower than the neighboring interpolar MTs, and that MT-flux is lost in spindles containing only KT-MTs (Mitchison *et al*, 2004). Moreover, this explains why kinesin-5 contribution to MT-flux is much stronger in *Xenopus* egg extracts spindles, in which most MTs are not associated with KTs (Miyamoto *et al*, 2004), as compared with spindles of human cells that contain a higher proportion of KT-MTs. Our finding that stable end-on KT-MT attachments work as flux brakes is also consistent with the “coupled spindle” model, in which fluxing non-KT-MTs transmit force to “passive” KT-MTs via MT-crosslinking (Matos *et al*, 2009). In agreement, we found that depletion of the MT-crosslinking proteins NuMA and HSET resulted in asynchronous MT-flux within different spindle MT subpopulations (Fig 4D and E). Instead of the signal smearing, the asynchrony in these kymograph tracks is represented by a few bifurcations. This points to the occurrence of rare, but more severe decoupling incidents, rather than to an increased frequency of small decoupling events. Since k-fibers are more bundled and therefore appear as the brightest signal within a kymograph, the asynchrony likely represents few k-fibers fluxing slower than the others. Although we cannot exclude the possibility that these effects arise from changes in overall spindle architecture, we favor the interpretation that MT-crosslinking molecules ensure the uniform distribution of spindle forces on metaphase chromosomes, enabling KT-MTs to flux due to coupling with non-KT-MTs (Fig 4F). Interestingly, chromosomes were shown to be dispensable for MT-flux in *Xenopus* egg extracts (Sawin & Mitchison, 1994), arguing against the role of chromatin in driving MT-flux. However, because the system lacked kinetochores as well (Sawin & Mitchison, 1994), it is reasonable to conceive that MT-flux depends on chromatin-based KIF4A only in the presence of stable end-on KT-MT attachments, as supported by the data presented in this study (Fig 5B). Our data are also in agreement with the “slide-and-cluster” model of spindle assembly, in which the chromatin-derived interpolar MTs undergo coordinated sliding toward the poles by a plus-end-directed motor, and clustering by a minus-end-directed motor (Burbank *et al*, 2007).

Several studies showed that MT-flux can be uncoupled from MT minus-end depolymerization (Waterman-Storer *et al*, 1998; Maiato *et al*, 2004; Dumont & Mitchison, 2009; Matos *et al*, 2009). Moreover, our data here demonstrate that CLASPs are dispensable for MT-flux in the absence of end-on KT-MT attachments (Fig 5B). These findings suggest that the MT growth-promoting activity of CLASPs and MT-depolymerizing activity of KIF2A, supported by MT-severing enzymes (Zhang *et al*, 2007; Jiang *et al*, 2017), act as MT-flux governing elements rather than its driving force.

In addition, our study shows that although MT-flux rate is in general positively correlated with spindle length, this correlation is lost in cells without stable end-on KT-MT attachments. Because MCAK depletion fully restored spindle length in metaphase cells with reduced MT-flux, we concluded that the role of MT-flux in human cells is to regulate mitotic spindle length in response to MCAK activity on KT-MTs. This explains why MT-flux becomes

dispensable to regulate spindle length in the absence of either MCAK (Ganem *et al*, 2005) or stable end-on KT-MT attachments (Fig 8A and C), and why overexpression of MCAK leads to substantially shorter spindles (Liao *et al*, 2019). Moreover, our model is also in agreement with previous work showing that ectopic enrichment of MCAK activity at centromeres attenuates MT-flux, reduces spindle length, and suppresses inter-KT tension (Wordeman *et al*, 2007). An appealing possibility is that MT-flux counteracts MCAK-dependent depolymerization of k-fibers by providing a bias for their plus-end polymerization. Indeed, when we attenuated the growth of k-fibers by depleting CLASPs, the k-fibers switched to MCAK-dependent depolymerization, which resulted in shorter spindles (Fig 8E). Thus, MT-flux might regulate the fine balance between MCAK-dependent depolymerization and CLASPs-promoting polymerization of k-fibers to ensure the steady-state length of the mitotic spindle. Interestingly, a recent elegant study used microneedle-based mechanical manipulation to pull on photomarked k-fibers and showed that the applied pulling force on KTs suppressed depolymerization of k-fibers, resulting in their elongation via MT plus-end polymerization (Long *et al*, 2020). Likewise, the sliding activities of four MT-flux driving motors might exert similar forces on KTs to promote MT plus-end polymerization. However, future work is required to address the precise molecular basis of this regulation, e.g., by dissecting whether MT-flux regulates the localization and/or activities of MCAK and CLASPs and whether the interplay between KT/centromere-localized kinases and phosphatases play an important regulatory role in this process.

In conclusion, our study demonstrates that MT-flux in human cells is driven by the coordinated action of four kinesins and is required to maintain mitotic spindle length by counteracting MCAK-mediated MT-depolymerizing activity on KT-MTs.

## Materials and Methods

### Cell culture, cloning, and plasmids

All cell lines were grown in Dulbecco's Modified Eagle Medium (DMEM) supplemented with 10% fetal bovine serum (FBS; Thermo Fisher Scientific) at 37°C in humidified conditions with 5% CO<sub>2</sub>. U2OS photoactivatable GFP (PA-GFP)- $\alpha$ -tubulin (Ganem *et al*, 2005) cell line expressing stable inducible short hairpin RNA (shKIF4A) targeting KIF4A sequence 5'-GCAAGATCCTGAAAGAGAT-3' was generated using a multipurpose GATEWAY-based lentiviral tetracycline-regulated conditional RNAi system (GLTR) using pENTR-THT-III (Addgene plasmid #55791) and pGLTR-X-Puro (Addgene plasmid #58246) plasmids (Sigl *et al*, 2014; Pfeiffenberger *et al*, 2016). Stable inducible U2OS PA-GFP- $\alpha$ -tubulin KIF4A shRNA cell lines conditionally expressing RNAi-resistant mCherry-KIF4A variants were generated by lentiviral infection followed by clonal selection with antibiotics.

The RNAi-resistant KIF4A and K94A motor mutant were generated using site-directed mutagenesis. RNAi targeting sequence 5'-GCAAGATCCTGAAAGAGAT-3' was mutated into 5'-GCAAGA TATTAAAAAGAGAT-3' (mutated nucleotides are underlined). Overlap extension PCR was used to generate KIF4A  $\Delta$ Zip1 mutant ( $\Delta$ 757–778) using RNAi-resistant KIF4A WT as a template and the following primers: KIF4A FWD: 5'-AAGGAAAAAAGCGGCCCAT GAAGGAAGAGGTGAAGGGA-3', KIF4A REV: 5'-CCGGATATCGTG

GGCCTCTTCTCGATAG-3', KIF4AΔZip1 FWD: 5'-AACGAAATTGAGGTTATGGTCAGTGCTCAACTCAAAGAAAAAAGGAA-3', and KIF4AΔZip1 REV: 5'-TTCCTTTTTTCTTTGAGTTGAGCACTGACCA TAACCTCAATTCGTA-3'. For Gateway cloning compatible N-terminal mCherry tagging of KIF4A, pENTR4-mCherry plasmid was generated by PCR amplification of the mCherry tag from pmCherry-C1 using the following primers mCh FWD: 5'-CGCGTTCGACATGGT GAGCAAGGGCGAGGA-3' and mCh REV: 5'-ACGCGGATCCCTTG TACAGCTCGTCCATGC-3' and ligating it into pENTR4 no cDB (gift from E. Campeau, Addgene plasmid #17424) plasmid (Campeau et al, 2009). The amplified PCR products of KIF4A variants were first cloned into pENTR4-mCherry and then sub-cloned into pLenti-CMV/TO-DEST (gift from E. Campeau, Addgene plasmid #17291) (Campeau et al, 2009) by LR recombination (Invitrogen) according to manufacturer's instructions. Production and expression of adenovirus encoding mCherry/mCherry-KIF4A was performed using pAd/CMV/V5-DEST Gateway Vector Kit (Thermo Fisher Scientific) according to manufacturer's instructions. The plasmids and corresponding mutations were verified by sequencing.

For rescue experiments, GFP-HSET and GFP-HSET N593K plasmids (gift from C. Walczak, Indiana University School of Medicine, USA) (Cai et al, 2009b) were transiently transfected (1 μg) for 24 h using Lipofectamine 2000 (Thermo Fisher Scientific) according to the manufacturer's protocol.

### Drug treatments

To induce monopolar spindles by inhibiting Eg5, 5 μM S-Trityl-L-Cysteine (STLC; Santa Cruz) was added to the medium 20 min before live-cell imaging, or 5 h before fixation. CENP-E was inhibited by adding 200 nM GSK923295 (Sigma-Aldrich) 20 min prior to imaging. DNA was labeled by adding 20 nM SiR-DNA (Spirochrome) 2 h prior to live-cell imaging. To inhibit MT-flux, 10 nM taxol (LC laboratories) was added to the medium for 30 min before live-cell imaging. To induce shRNA-mediated depletion of Kif4A and simultaneous expression of its respective RNAi-resistant variants, 1 μg/ml of doxycycline (Sigma-Aldrich) was added to the refreshed medium each day for 2 days.

### Mitosis with unreplicated genomes

Mitosis with unreplicated genomes was induced as described previously (Schlegel & Pardee, 1986; Wise & Brinkley, 1997). Briefly, U2OS cells stably expressing PA-GFP/mCherry- $\alpha$ -tubulin (gift from R. Medema, NKI, Amsterdam, the Netherlands) (van Heesbeen et al, 2014) were first synchronized in mitosis with 2 μM nocodazole (Sigma-Aldrich) for 16 h. Mitotic cells were collected by shake-off, washed in DMEM and plated at a density  $4.5 \times 10^5$  cells in 35 mm glass-bottomed dish (14 mm, No. 1.5, MatTek Corporation). To inhibit DNA replication, 2 mM hydroxyurea (HU; Sigma-Aldrich) was added directly to the cell culture medium for 23 h. Next day, the medium was replaced with fresh medium containing 2 mM HU and 5 mM caffeine and incubated for an additional 6 h.

### RNAi interference

U2OS cells stably expressing PA-GFP/mCherry- $\alpha$ -tubulin (van Heesbeen et al, 2014) were transfected with 50 nM siRNAs for 48–72 h,

using Lipofectamine RNAiMAX (Thermo Fisher Scientific). The siRNAs used in this study are: KIF4A, 5'-GCAGAUUGAAAGCCUAG AG-3' (Wandke et al, 2012); KIF2A, 5'-GGCAAAGAGAUUGACCU GG-3' (Ganem & Compton, 2004); hKID, 5'-CAAGCUCACUCGCCUA UUGTT-3' (Wolf et al, 2006; Wandke et al, 2012); KIF15, 5'-GGA CAUAAAUUGCAAUACTT-3' (Tanenbaum et al, 2009); CLASP1, 5'-GGAUGAUUUACAAGACUGG-3' (Mimori-Kiyosue et al, 2006); CLASP2, 5'-GACAUACAUGGGUCUUAGA-3' (Mimori-Kiyosue et al, 2006); NDC80, 5'-GAAUUGCAGCAGACUAUUA-3'; NuMA, 5'-AAG GGCGCAAACAGAGCACUA-3' (Kotak et al, 2012); HSET, 5'-UCAGA AGCAGCCCUGUCA-3' (Cai et al, 2009b); PRC1, 5'-AAAUAUGGGA GCUAAUUGGGA-3' (Mollinari et al, 2002); MCAK, 5'-GAUCCAACG CAGUAAUGGU-3' (Cassimeris & Morabito, 2004) and non-targeting control siRNA (D-001810-01-05, Dharmacon Inc.), 5'-UGGUUACA UGUCGACUAA-3'. For rescue experiments of HSET, U2OS cells stably expressing mEOS- $\alpha$ -tubulin (Wandke et al, 2012) were transfected with 100 nM siRNA targeting 3'UTR for HSET, 5'-CAUGUCC CAGGGCUAUCAAA-3' (Cai et al, 2009b).

### Immunoblotting and immunofluorescence

For immunoblotting, cells following subjected treatments were collected and lysed in NP40 buffer (50 mM Tris-HCl pH 8, 150 mM NaCl, 5 mM EDTA, 0.5% NP-40, 1× EDTA-free protease inhibitor [Sigma-Aldrich], 1× phosphatase inhibitor cocktail [Sigma-Aldrich], 1 mM PMSF) by two cycles of freezing and thawing using liquid N<sub>2</sub>. Protein extracts collected after centrifugation were subjected to SDS-PAGE and transferred onto nitrocellulose membrane (Bio-Rad). After blocking with PBS containing 0.1% Tween-20 and 5% milk, membranes were incubated overnight with primary antibodies, washed in PBS containing 0.1% Tween-20, and then incubated 1 h with HRP-conjugated secondary antibodies (Jackson ImmunoResearch). After washing with PBS containing 0.1% Tween-20, immunodetection was performed with ECL (Bio-Rad). Immunoblots were performed using the following primary antibodies: rabbit anti-KIF15 (1:1,000; Cytoskeleton Inc., Cat#AKIN13), rabbit anti-KIF2A (1:1,000; Novus Biologicals, NB500-180); rabbit anti-KIF4A (1:1,000) (Wandke et al, 2012), mouse anti-hKID (8C12; 1:1,000) (Wandke & Geley, 2006); rat anti-CLASP1 (1:200) and rat anti-CLASP2 (1:200) (Maffini et al, 2009), mouse anti-PRC1 (C-1; 1:500; Santa Cruz, sc-3769839), mouse anti-NDC80/HEC1 (1:2,000; Nordic Biosite, GTX70268), mouse anti-NuMA (F-11; 1:250; Santa Cruz, sc-365532), rabbit anti-HSET (1:500; Bethyl, A300-951A), mouse anti-MCAK (1:1,000; Abnova H00011004-M01), mouse anti-Vinculin (1:5,000; Sigma-Aldrich, SAB4200729, Vin-11-5), mouse anti- $\alpha$ -tubulin (1:10,000; Sigma-Aldrich T5168, B-5-1-2), mouse anti-GAPDH (1:25,000; Proteintech 60004-1-Ig), HRP-conjugated secondary antibodies (1:10,000; Jackson ImmunoResearch), and visualized by ECL (Bio-Rad).

For immunofluorescence, U2OS cells grown on glass coverslips were fixed either by ice-cold methanol for 4 min at -20°C, or by 4% paraformaldehyde in PHEM buffer for 20 min at 37°C as described before (DeLuca, 2010). Cells were washed with 1× phosphate-buffered saline (PBS) and immunostained with primary and Alexa Fluor-conjugated secondary antibodies diluted in IF stain (1× PBS, 1% FBS, 0.5% Tween). DNA was counterstained with DAPI (Sigma-Aldrich, final concentration 0.1 μg/ml) and mounted on glass slides using Fluoromount-G mounting media (Southern



Biotech). Images were acquired using LSM700 confocal microscope (Carl Zeiss Microimaging Inc.) mounted on a Zeiss Axio imager Z1 equipped with plan-apochromat 63×/1.40 oil DIC M27 objective (Carl Zeiss, Inc.) and Zen 2008 software (Carl Zeiss, Inc.). Primary antibodies used were mouse anti- $\alpha$ -tubulin (DM1A; 1:2,000; Sigma-Aldrich, T9026), rabbit anti- $\alpha$ -tubulin (1:500; Abcam, ab15246); rabbit anti-KIF4A (1:500; Bethyl, A301-074A), rabbit anti-CENP-E (1:500, Abcam, ab133583), and mouse anti-PRC1 (1:250; Santa Cruz, sc-3769839) and the Alexa Fluor-conjugated secondary antibodies (1:1,000; Thermo Fisher Scientific).

### Live-cell imaging

Time-lapse imaging was performed in a heated incubation chamber at 37°C with controlled humidity and 5% CO<sub>2</sub> supply using a Plan-Apochromat 63x/1.4NA oil objective with differential interference contrast mounted on an inverted Zeiss Axio Observer Z1 microscope (Marianas Imaging Workstation [3i—Intelligent Imaging Innovations, Inc., Denver, CO, USA]), equipped with a CSU-X1 spinning disk confocal head (Yokogawa Corporation of America) and four laser lines (405, 488, 561, and 640 nm). Images were acquired using an iXon Ultra 888 EM-CCD camera (Andor Technology). Fifteen 1  $\mu$ m-separated z-planes were collected every 1 min for 2 h. Cells with collapsing spindles (e.g., STLC-treated and KIF15-depleted) were discarded from quantifications of MT-flux and spindle length in bipolar spindles and only the ones that maintained spindle length during filming were quantified.

To quantify the spindle length, the distance between mCherry-labeled spindle poles was measured in 3D using ImageJ (National Institute of Health, Bethesda, MD, USA). For MCAK RNAi-mediated recovery experiments, the spindle length was quantified using time-lapse images of mitotic spindles with fifteen 1  $\mu$ m-separated z-planes imaged every 2 min.

### Photoactivation and MT-flux analysis

For the MT poleward flux measurement, photoactivation and photo-conversion experiments were performed using U2OS-PA-GFP/mCherry- $\alpha$ -tubulin (van Heesbeen *et al*, 2014), U2OS-PA-GFP (Ganem *et al*, 2005), and U2OS-mEOS- $\alpha$ -tubulin (Wandke *et al*, 2012) cell lines, cultured in 35 mm glass-bottomed dishes (14 mm, No. 1.5, MatTek Corporation). Fluorescent signals of SiR-DNA and mCherry- $\alpha$ -tubulin were used to differentiate between early prometaphase and metaphase cells. Two transversal line-shaped regions of interest, placed perpendicular to the main spindle axis on both sides of the metaphase plate, were photoactivated using a laser-based point scanner (Vector, 3i—Intelligent Imaging Innovations, Inc., Denver, CO, USA) in bipolar spindles, while 2–3 concentric rings were used for photoactivation of monopolar spindles. Photoactivation was carried out by one 5 ms pulse from a 405 nm laser. Images were acquired every 5 s for 4 min over three 0.5  $\mu$ m-separated z-planes. Kymograph generation and velocity quantification were performed using a custom-written MATLAB script (Pereira & Maiato, 2010). Initially, the spindle is stabilized by tracking the spindle poles, the coordinates of which are looked up to rotate and translate the rectangular ROIs covering the whole spindle for the definition of each kymograph layer. Each layer (a matrix) is then collapsed into a vector using a projection criteria (maximum or

sum), generating a collapsed kymograph such as the ones shown in Fig 1D. To calculate flux velocity, a sparse set of manually chosen points is used as a first guess for stripe position at specific points. This initial estimate is made continuous by computing a cubic spline curve. Within a preset neighborhood, the position of the stripe at each time point is then corrected by calculating an intensity-based centroid. Finally, a linear fit is performed to these corrected positions, the slope of which is the stripe velocity averaged over the time window used to generate the kymograph. In fact, two stripes are imprinted in each cell, the velocities of which (one positive and one negative) are subtracted and then halved to yield a poleward flux velocity relative to a virtual spindle equator, which is used as the final readout presented in quantifications.

### CH-STED microscopy

U2OS cells grown on glass coverslips and HeLa cells stably expressing a bacterial artificial chromosome encoding mouse CENP-E-GFP (LAP) under control of its own promoter and low copy number (Poser *et al*, 2008) grown on fibronectin-coated coverslips were fixed using a solution of 4% paraformaldehyde (Electron microscopy sciences) and 0.1% glutaraldehyde (Electron microscopy sciences) for 10 min at RT. Autofluorescence was quenched using freshly prepared 0.01% sodium borohydride for 7 min at RT. Cells were permeabilized with 0.5% Triton X-100 in PBS for 10 min at RT, washed, and incubated in blocking solution (10% fetal bovine serum [FBS] in 0.05% PBS-Tween) for 30 min. Immunolabeling was performed with the following primary antibodies: rabbit anti-CENP-E (1:25, Abcam, ab133583), rabbit anti-KIF4A (1:50; PA5-30492, Thermo Scientific), rat anti-tyrosinated tubulin (1:100, MCA77G, AbD Serotec), guinea pig anti-CENP-C (1:500, PD030, MBL International), rabbit anti-GFP (1:100; house made), mouse anti- $\alpha$ -tubulin (1:500; clone B512, Sigma); and the following fluorescently labeled secondary antibodies: anti-rabbit 580 STAR (1:100; Abberior), anti-rat STAR RED (1:100, Abberior), anti-mouse 635p STAR (1:100; Abberior), Alexa Fluor-488 (1:1,000, Thermo Fisher Scientific), and DAPI (1  $\mu$ g/ml) as DNA counterstain. CH-STED microscopy was performed as described previously (Pereira *et al*, 2019). Briefly, CH-STED uses a bivortex phase mask that generates a depletion beam with a tunable dip and high resilience to spherical and the other “radial” aberrations. Essentially, CH-STED differs from conventional 2D-STED in that it creates an axially concave excitation point-spread function, meaning that the fluorophores at the focal plane region become the preferential source of fluorescence. This qualitative change provides optical sectioning without a pinhole. If a confocal pinhole is indeed used at the detection side, as in the case of this study, the two sectioning contributions operate serially, mutually reinforcing background reduction. An Abberior Instruments “Expert Line” gated-STED was used coupled to a Nikon Ti microscope with 60× 1.4NA Plan-Apo objective (Nikon, Lambda Series) oil-immersion, pinhole size of 0.8 Airy units, 40 MHz modulated excitation (405, 488, 560, and 640 nm) and depletion (775 nm) lasers. Abberior’s Inspector software was used to control the acquisition process.

### Quantification and statistical analysis

Statistical analysis and graphs were generated in GraphPad Prism 8.0. Statistical details of experiments and tests used are indicated in the figure legends. The data points were tested for normality using

Shapiro–Wilk test. Accordingly, statistical significance was determined by Student's *t*-test (unpaired, two-tailed) or one-way ANOVA with Dunnett's *post hoc* test for data sets that followed a normal distribution pattern. For data sets that significantly deviated from a normal distribution, Mann–Whitney *U*-test (unpaired, two-tailed) or Kruskal–Wallis *H*-test with Dunn's *post hoc* test were used. For parametric tests, *F*-test was used to compare variances and Welch's correction was employed for conditions that did not have equal variances. Details of the statistical significance and *n* values for each condition can be found in the figures and figure legends.

## Data availability

This study includes no data deposited in external repositories.

**Expanded View** for this article is available online.

## Acknowledgements

We thank Duane Compton and Rene Medema for providing the U2OS PA-GFP-tubulin and U2OS PA-GFP-tubulin/mCherry-tubulin cell lines, respectively. We thank Claire Walczak for providing the GFP-HSET and GFP-HSET N593K plasmids. We thank Martina Barisic for technical assistance. Work in the laboratory of MB is supported by grants from the Danish Cancer Society Scientific Committee (KBVU; R146-A9322), the Lundbeck Foundation (R215-2015-4081), and the Novo Nordisk Foundation (NNF19OC0058504). Work in the laboratory of HM is funded by the European Research Council (grant agreement No 681443) under the European Union's Horizon 2020 research and innovation program.

## Author contributions

YS, GR, AJP, HM, and MB designed experiments; YS generated tools and performed and analyzed most of the experiments; YS and MB performed photoactivation experiments, image quantification, and analysis. GR performed and analyzed the spindle length-related experiments. MO performed and analyzed initial photoactivation experiments; YS, AJP, and HM performed CH-STED experiments and analysis; SG and AJ provided reagents; SE contributed to designing and analyzing the experiments; MB, YS, and GR wrote the manuscript, with contributions from all authors; MB conceived and coordinated the project.

## Conflict of interest

The authors declare that they have no conflict of interest.

## References

- Antonio C, Ferby I, Wilhelm H, Jones M, Karsenti E, Nebreda AR, Vernos I (2000) Xkid, a chromokinesin required for chromosome alignment on the metaphase plate. *Cell* 102: 425–435
- Bajer AS, Molè-Bajer J (1972) Spindle dynamics and chromosome movements. *Int Rev Cytol Supplement* 3: 271
- Barisic M, Aguiar P, Geley S, Maiato H (2014) Kinetochore motors drive congression of peripheral polar chromosomes by overcoming random arm-ejection forces. *Nat Cell Biol* 16: 1249–1256
- Barisic M, Silva e Sousa R, Tripathy SK, Magiera MM, Zaytsev AV, Pereira AL, Janke C, Grishchuk EL, Maiato H (2015) Mitosis. Microtubule detyrosination guides chromosomes during mitosis. *Science* 348: 799–803
- Brinkley BR, Zinkowski RP, Mollon WL, Davis FM, Pisegna MA, Pershouse M, Rao PN (1988) Movement and segregation of kinetochores experimentally detached from mammalian chromosomes. *Nature* 336: 251–254
- Brouhard GJ, Hunt AJ (2005) Microtubule movements on the arms of mitotic chromosomes: polar ejection forces quantified *in vitro*. *Proc Natl Acad Sci USA* 102: 13903–13908
- Brust-Mascher I, Scholey JM (2002) Microtubule flux and sliding in mitotic spindles of *Drosophila* embryos. *Mol Biol Cell* 13: 3967–3975
- Burbank KS, Mitchison TJ, Fisher DS (2007) Slide-and-cluster models for spindle assembly. *Curr Biol* 17: 1373–1383
- Cai S, O'Connell CB, Khodjakov A, Walczak CE (2009a) Chromosome congression in the absence of kinetochore fibres. *Nat Cell Biol* 11: 832–838
- Cai S, Weaver LN, Ems-McClung SC, Walczak CE (2009b) Kinesin-14 family proteins HSET/XCTK2 control spindle length by cross-linking and sliding microtubules. *Mol Biol Cell* 20: 1348–1359
- Cameron LA, Yang G, Cimini D, Canman JC, Kisurina-Evgenieva O, Khodjakov A, Danuser G, Salmon ED (2006) Kinesin 5-independent poleward flux of kinetochore microtubules in PtK1 cells. *J Cell Biol* 173: 173–179
- Campeau E, Ruhl VE, Rodier F, Smith CL, Rahmberg BL, Fuss JO, Campisi J, Yaswen P, Cooper PK, Kaufman PD (2009) A versatile viral system for expression and depletion of proteins in mammalian cells. *PLoS ONE* 4: e6529
- Cassimeris L, Morabito J (2004) TOGp, the human homolog of XMAP215/Dis1, is required for centrosome integrity, spindle pole organization, and bipolar spindle assembly. *Mol Biol Cell* 15: 1580–1590
- Chakraborty M, Tarasovets EV, Zaytsev AV, Godzi M, Figueiredo AC, Ataulkhanov FI, Grishchuk EL (2019) Microtubule end conversion mediated by motors and diffusing proteins with no intrinsic microtubule end-binding activity. *Nat Commun* 10: 1673
- Cheeseman IM, Chappie JS, Wilson-Kubalek EM, Desai A (2006) The conserved KMN network constitutes the core microtubule-binding site of the kinetochore. *Cell* 127: 983–997
- DeLuca JG, Moree B, Hickey JM, Kilmartin JV, Salmon ED (2002) hNuf2 inhibition blocks stable kinetochore-microtubule attachment and induces mitotic cell death in HeLa cells. *J Cell Biol* 159: 549–555
- DeLuca JG (2010) Kinetochore-microtubule dynamics and attachment stability. *Methods Cell Biol* 97: 53–79
- Desai A, Verma S, Mitchison TJ, Walczak CE (1999) Kin I kinesins are microtubule-destabilizing enzymes. *Cell* 96: 69–78
- Dong Z, Zhu C, Zhan Q, Jiang W (2018) Cdk phosphorylation licenses Kif4A chromosome localization required for early mitotic progression. *J Mol Cell Biol* 10: 358–370
- Drechsler H, McHugh T, Singleton MR, Carter NJ, McAinsh AD (2014) The Kinesin-12 Kif15 is a processive track-switching tetramer. *Elife* 3: e01724
- Dumont S, Mitchison TJ (2009) Compression regulates mitotic spindle length by a mechanochemical switch at the poles. *Curr Biol* 19: 1086–1095
- Ems-McClung SC, Walczak CE (2010) Kinesin-13s in mitosis: key players in the spatial and temporal organization of spindle microtubules. *Semin Cell Dev Biol* 21: 276–282
- Forer A (1965) Local reduction of spindle fiber birefringence in living nephrotoma suturalis (Loew) spermatocytes induced by ultraviolet microbeam irradiation. *J Cell Biol* 25(SUPPL): 95–117
- Fu J, Bian M, Xin G, Deng Z, Luo J, Guo X, Chen H, Wang Y, Jiang Q, Zhang C (2015) TPX2 phosphorylation maintains metaphase spindle length by regulating microtubule flux. *J Cell Biol* 210: 373–383
- Funabiki H, Murray AW (2000) The *Xenopus* chromokinesin Xkid is essential for metaphase chromosome alignment and must be degraded to allow anaphase chromosome movement. *Cell* 102: 411–424

- Gaetz J, Kapoor TM (2004) Dynein/dynactin regulate metaphase spindle length by targeting depolymerizing activities to spindle poles. *J Cell Biol* 166: 465–471
- Ganem NJ, Compton DA (2004) The KinI kinesin Kif2a is required for bipolar spindle assembly through a functional relationship with MCAK. *J Cell Biol* 166: 473–478
- Ganem NJ, Upton K, Compton DA (2005) Efficient mitosis in human cells lacking poleward microtubule flux. *Curr Biol* 15: 1827–1832
- Girao H, Okada N, Rodrigues TA, Silva AO, Figueiredo AC, Garcia Z, Moutinho-Santos T, Hayashi I, Azevedo JE, Macedo-Ribeiro S et al (2020) CLASP2 binding to curved microtubule tips promotes flux and stabilizes kinetochore attachments. *J Cell Biol* 219: e201905080
- Hamaguchi Y, Toriyama M, Sakai H, Hiramoto Y (1987) Redistribution of fluorescently labeled tubulin in the mitotic apparatus of sand dollar eggs and the effects of taxol. *Cell Struct Funct* 12: 43–52
- van Heesbeen RG, Tanenbaum ME, Medema RH (2014) Balanced activity of three mitotic motors is required for bipolar spindle assembly and chromosome segregation. *Cell Rep* 8: 948–956
- Hiramoto Y, Izutsu K (1977) Poleward movement of “markers” existing in mitotic spindles of grasshopper spermatocytes. *Cell Struct Funct* 2: 257–259
- Howell BJ, McEwen BF, Canman JC, Hoffman DB, Farrar EM, Rieder CL, Salmon ED (2001) Cytoplasmic dynein/dynactin drives kinetochore protein transport to the spindle poles and has a role in mitotic spindle checkpoint inactivation. *J Cell Biol* 155: 1159–1172
- Hu CK, Ozlu N, Coughlin M, Steen JJ, Mitchison TJ (2012) Plk1 negatively regulates PRC1 to prevent premature midzone formation before cytokinesis. *Mol Biol Cell* 23: 2702–2711
- Hueschen CL, Kenny SJ, Xu K, Dumont S (2017) NuMA recruits dynein activity to microtubule minus-ends at mitosis. *Elife* 6: e29328
- Itoh G, Ikeda M, Iemura K, Amin MA, Kuriyama S, Tanaka M, Mizuno N, Osakada H, Haraguchi T, Tanaka K (2018) Lateral attachment of kinetochores to microtubules is enriched in prometaphase rosette and facilitates chromosome alignment and bi-orientation establishment. *Sci Rep* 8: 3888
- Jiang K, Rezabkova L, Hua S, Liu Q, Capitani G, Altelaar AFM, Heck AJR, Kammerer RA, Steinmetz MO, Akhmanova A (2017) Microtubule minus-end regulation at spindle poles by an ASPM-katanin complex. *Nat Cell Biol* 19: 480–492
- Kajtez J, Solomatina A, Novak M, Polak B, Vukusic K, Rudiger J, Cojoc G, Milas A, Sumanovac Sestak I, Risteski P et al (2016) Overlap microtubules link sister k-fibres and balance the forces on bi-oriented kinetochores. *Nat Commun* 7: 10298
- Kapoor TM, Mayer TU, Coughlin ML, Mitchison TJ (2000) Probing spindle assembly mechanisms with monastrol, a small molecule inhibitor of the mitotic kinesin, Eg5. *J Cell Biol* 150: 975–988
- Kapoor TM, Lampson MA, Hergert P, Cameron L, Cimini D, Salmon ED, McEwen BF, Khodjakov A (2006) Chromosomes can congress to the metaphase plate before biorientation. *Science* 311: 388–391
- Kotak S, Busso C, Gonczy P (2012) Cortical dynein is critical for proper spindle positioning in human cells. *J Cell Biol* 199: 97–110
- Kurasawa Y, Earnshaw WC, Mochizuki Y, Dohmae N, Todokoro K (2004) Essential roles of KIF4 and its binding partner PRC1 in organized central spindle midzone formation. *EMBO J* 23: 3237–3248
- LaFountain JR Jr, Cohan CS, Siegel AJ, LaFountain DJ (2004) Direct visualization of microtubule flux during metaphase and anaphase in crane-fly spermatocytes. *Mol Biol Cell* 15: 5724–5732
- Lecland N, Luders J (2014) The dynamics of microtubule minus ends in the human mitotic spindle. *Nat Cell Biol* 16: 770–778
- Levesque AA, Compton DA (2001) The chromokinesin Kid is necessary for chromosome arm orientation and oscillation, but not congression, on mitotic spindles. *J Cell Biol* 154: 1135–1146
- Liao S, Rajendraprasad G, Wang N, Eibes S, Gao J, Yu H, Wu G, Tu X, Huang H, Barisic M et al (2019) Molecular basis of vasohibins-mediated detyrosination and its impact on spindle function and mitosis. *Cell Res* 29: 533–547
- Logarinho E, Maffini S, Barisic M, Marques A, Toso A, Meraldi P, Maiato H (2012) CLASPs prevent irreversible multipolarity by ensuring spindle-pole resistance to traction forces during chromosome alignment. *Nat Cell Biol* 14: 295–303
- Long AF, Suresh P, Dumont S (2020) Individual kinetochore-fibers locally dissipate force to maintain robust mammalian spindle structure. *J Cell Biol* 219: e201911090
- Maddox P, Straight A, Coughlin P, Mitchison TJ, Salmon ED (2003) Direct observation of microtubule dynamics at kinetochores in *Xenopus* extract spindles: implications for spindle mechanics. *J Cell Biol* 162: 377–382
- Maffini S, Maia AR, Manning AL, Maliga Z, Pereira AL, Junqueira M, Shevchenko A, Hyman A, Yates JR 3rd, Galjart N et al (2009) Motor-independent targeting of CLASPs to kinetochores by CENP-E promotes microtubule turnover and poleward flux. *Curr Biol* 19: 1566–1572
- Maiato H, Rieder CL, Khodjakov A (2004) Kinetochore-driven formation of kinetochore fibers contributes to spindle assembly during animal mitosis. *J Cell Biol* 167: 831–840
- Maiato H, Khodjakov A, Rieder CL (2005) *Drosophila* CLASP is required for the incorporation of microtubule subunits into fluxing kinetochore fibres. *Nat Cell Biol* 7: 42–47
- Matos I, Pereira AJ, Lince-Faria M, Cameron LA, Salmon ED, Maiato H (2009) Synchronizing chromosome segregation by flux-dependent force equalization at kinetochores. *J Cell Biol* 186: 11–26
- Mazumdar M, Sundareshan S, Misteli T (2004) Human chromokinesin KIF4A functions in chromosome condensation and segregation. *J Cell Biol* 166: 613–620
- McClelland ML, Gardner RD, Kallio MJ, Daum JR, Gorbisky GJ, Burke DJ, Stukenberg PT (2003) The highly conserved Ndc80 complex is required for kinetochore assembly, chromosome congression, and spindle checkpoint activity. *Genes Dev* 17: 101–114
- Merdes A, Ramyar K, Vechio JD, Cleveland DW (1996) A complex of NuMA and cytoplasmic dynein is essential for mitotic spindle assembly. *Cell* 87: 447–458
- Mimori-Kiyosue Y, Grigoriev I, Sasaki H, Matsui C, Akhmanova A, Tsukita S, Vorobjev I (2006) Mammalian CLASPs are required for mitotic spindle organization and kinetochore alignment. *Genes Cells* 11: 845–857
- Mitchison TJ (1989) Polewards microtubule flux in the mitotic spindle: evidence from photoactivation of fluorescence. *J Cell Biol* 109: 637–652
- Mitchison TJ, Maddox P, Groen A, Cameron L, Perlman Z, Ohi R, Desai A, Salmon ED, Kapoor TM (2004) Bipolarization and poleward flux correlate during *Xenopus* extract spindle assembly. *Mol Biol Cell* 15: 5603–5615
- Miyamoto DT, Perlman ZE, Burbank KS, Groen AC, Mitchison TJ (2004) The kinesin Eg5 drives poleward microtubule flux in *Xenopus laevis* egg extract spindles. *J Cell Biol* 167: 813–818
- Mollinari C, Kleman JP, Jiang W, Schoehn G, Hunter T, Margolis RL (2002) PRC1 is a microtubule binding and bundling protein essential to maintain the mitotic spindle midzone. *J Cell Biol* 157: 1175–1186
- Mountain V, Simerly C, Howard L, Ando A, Schatten G, Compton DA (1999) The kinesin-related protein, HSET, opposes the activity of Eg5 and cross-links microtubules in the mammalian mitotic spindle. *J Cell Biol* 147: 351–366



- Nguyen PA, Field CM, Mitchison TJ (2018) Prc1E and Kif4A control microtubule organization within and between large *Xenopus* egg asters. *Mol Biol Cell* 29: 304–316
- O'Connell CB, Loncarek J, Hergert P, Kourtidis A, Conklin DS, Khodjakov A (2008) The spindle assembly checkpoint is satisfied in the absence of interkinetochore tension during mitosis with unreplicated genomes. *J Cell Biol* 183: 29–36
- Pereira A, Sousa M, Almeida AC, Ferreira LT, Costa AR, Novais-Cruz M, Ferras C, Sousa MM, Sampaio P, Belsley M et al (2019) Coherent-hybrid STED: high contrast sub-diffraction imaging using a bi-vortex depletion beam. *Opt Express* 27: 8092–8111
- Pereira AJ, Maiato H (2010) Improved kymography tools and its applications to mitosis. *Methods* 51: 214–219
- Pereira AJ, Maiato H (2012) Maturation of the kinetochore-microtubule interface and the meaning of metaphase. *Chromosome Res* 20: 563–577
- Pfeifferberger E, Sigl R, Geley S (2016) Conditional RNAi Using the Lentiviral GLTR System. *Methods Mol Biol* 1448: 121–138
- Polak B, Risteski P, Lesjak S, Tolic IM (2017) PRC1-labeled microtubule bundles and kinetochore pairs show one-to-one association in metaphase. *EMBO Rep* 18: 217–230
- Poser I, Sarov M, Hutchins JR, Heriche JK, Toyoda Y, Pozniakovskiy A, Weigl D, Nitzsche A, Hegemann B, Bird AW et al (2008) BAC TransgeneOmics: a high-throughput method for exploration of protein function in mammals. *Nat Methods* 5: 409–415
- Radulescu AE, Cleveland DW (2010) NuMA after 30 years: the matrix revisited. *Trends Cell Biol* 20: 214–222
- Renda F, Pellacani C, Strunov A, Bucciarelli E, Naim V, Bosso G, Kiseleva E, Bonaccorsi S, Sharp DJ, Khodjakov A et al (2017) The *Drosophila* orthologue of the INT6 onco-protein regulates mitotic microtubule growth and kinetochore structure. *PLoS Genet* 13: e1006784
- Rieder CL, Davison EA, Jensen LC, Cassimeris L, Salmon ED (1986) Oscillatory movements of mono-oriented chromosomes and their position relative to the spindle pole result from the ejection properties of the aster and half-spindle. *J Cell Biol* 103: 581–591
- Rieder CL, Salmon ED (1994) Motile kinetochores and polar ejection forces dictate chromosome position on the vertebrate mitotic spindle. *J Cell Biol* 124: 223–233
- Rogers GC, Rogers SL, Schwimmer TA, Ems-McClung SC, Walczak CE, Vale RD, Scholey JM, Sharp DJ (2004) Two mitotic kinesins cooperate to drive sister chromatid separation during anaphase. *Nature* 427: 364–370
- Sawin KE, Mitchison TJ (1991) Poleward microtubule flux mitotic spindles assembled *in vitro*. *J Cell Biol* 112: 941–954
- Sawin KE, Mitchison TJ (1994) Microtubule flux in mitosis is independent of chromosomes, centrosomes, and antiparallel microtubules. *Mol Biol Cell* 5: 217–226
- Schaar BT, Chan GK, Maddox P, Salmon ED, Yen TJ (1997) CENP-E function at kinetochores is essential for chromosome alignment. *J Cell Biol* 139: 1373–1382
- >Schlegel R, Pardee AB (1986) Caffeine-induced uncoupling of mitosis from the completion of DNA replication in mammalian cells. *Science* 232: 1264–1266
- Shimamoto Y, Maeda YT, Ishiwata S, Libchaber AJ, Kapoor TM (2011) Insights into the micromechanical properties of the metaphase spindle. *Cell* 145: 1062–1074
- Shrestha RL, Draviam VM (2013) Lateral to end-on conversion of chromosome-microtubule attachment requires kinesins CENP-E and MCAK. *Curr Biol* 23: 1514–1526
- Sigl R, Ploner C, Shivalingaiah G, Kofler R, Geley S (2014) Development of a multipurpose GATEWAY-based lentiviral tetracycline-regulated conditional RNAi system (GLTR). *PLoS ONE* 9: e97764
- Sikirzhyski V, Renda F, Tikhonenko I, Magidson V, McEwen BF, Khodjakov A (2018) Microtubules assemble near most kinetochores during early prometaphase in human cells. *J Cell Biol* 217: 2647–2659
- Suresh P, Long AF, Dumont S (2020) Microneedle manipulation of the mammalian spindle reveals specialized, short-lived reinforcement near chromosomes. *Elife* 9: e53807
- Tanenbaum ME, Macurek L, Janssen A, Geers EF, Alvarez-Fernandez M, Medema RH (2009) Kif15 cooperates with eg5 to promote bipolar spindle assembly. *Curr Biol* 19: 1703–1711
- Tipton AR, Wren JD, Daum JR, Siefert JC, Gorbisky GJ (2017) GTSE1 regulates spindle microtubule dynamics to control Aurora B kinase and Kif4A chromokinesin on chromosome arms. *J Cell Biol* 216: 3117–3132
- Vernos I, Raats J, Hirano T, Heasman J, Karsenti E, Wylie C (1995) Xklp1, a chromosomal *Xenopus* kinesin-like protein essential for spindle organization and chromosome positioning. *Cell* 81: 117–127
- Vladimirov E, McHedlishvili N, Gasic I, Armond JW, Samora CP, Meraldi P, McAinsh AD (2013) Nonautonomous movement of chromosomes in mitosis. *Dev Cell* 27: 60–71
- Vukusic K, Buda R, Bosilj A, Milas A, Pavin N, Tolic IM (2017) Microtubule sliding within the bridging fiber pushes kinetochore fibers apart to segregate chromosomes. *Dev Cell* 43: 11–23.e16
- Vukušić K, Buđa R, Ponjavić I, Risteski P, Tolić IM (2019) Chromosome segregation is driven by joint microtubule sliding action of kinesins KIF4A and EG5. *bioRxiv*, 863381 <https://doi.org/10.1101/863381> [PREPRINT]
- Wandke C, Geley S (2006) Generation and characterization of an hKid-specific monoclonal antibody. *Hybridoma (Larchmt)* 25: 41–43
- Wandke C, Barisic M, Sigl R, Rauch V, Wolf F, Amaro AC, Tan CH, Pereira AJ, Kutay U, Maiato H et al (2012) Human chromokinesins promote chromosome congression and spindle microtubule dynamics during mitosis. *J Cell Biol* 198: 847–863
- Waterman-Storer CM, Desai A, Bulinski JC, Salmon ED (1998) Fluorescent speckle microscopy, a method to visualize the dynamics of protein assemblies in living cells. *Curr Biol* 8: 1227–1230
- Wei RR, Al-Bassam J, Harrison SC (2007) The Ndc80/HEC1 complex is a contact point for kinetochore-microtubule attachment. *Nat Struct Mol Biol* 14: 54–59
- Wigge PA, Kilmartin JV (2001) The Ndc80p complex from *Saccharomyces cerevisiae* contains conserved centromere components and has a function in chromosome segregation. *J Cell Biol* 152: 349–360
- Wise DA, Brinkley BR (1997) Mitosis in cells with unreplicated genomes (MUGs): spindle assembly and behavior of centromere fragments. *Cell Motil Cytoskeleton* 36: 291–302
- Wolf F, Wandke C, Isenberg N, Geley S (2006) Dose-dependent effects of stable cyclin B1 on progression through mitosis in human cells. *EMBO J* 25: 2802–2813
- Wood KW, Sakowicz R, Goldstein LS, Cleveland DW (1997) CENP-E is a plus end-directed kinetochore motor required for metaphase chromosome alignment. *Cell* 91: 357–366
- Wordeman L, Wagenbach M, von Dassow G (2007) MCAK facilitates chromosome movement by promoting kinetochore microtubule turnover. *J Cell Biol* 179: 869–879
- Wu G, Chen PL (2008) Structural requirements of chromokinesin Kif4A for its proper function in mitosis. *Biochem Biophys Res Commun* 372: 454–458

Yen TJ, Compton DA, Wise D, Zinkowski RP, Brinkley BR, Earnshaw WC, Cleveland DW (1991) CENP-E, a novel human centromere-associated protein required for progression from metaphase to anaphase. *EMBO J* 10: 1245–1254

Zhang D, Rogers GC, Buster DW, Sharp DJ (2007) Three microtubule severing enzymes contribute to the “Pacman-flux” machinery that moves chromosomes. *J Cell Biol* 177: 231–242

Zhu C, Jiang W (2005) Cell cycle-dependent translocation of PRC1 on the spindle by Kif4 is essential for midzone formation and cytokinesis. *Proc Natl Acad Sci USA* 102: 343–348

Zhu C, Lau E, Schwarzenbacher R, Bossy-Wetzel E, Jiang W (2006) Spatiotemporal control of spindle midzone formation by PRC1 in human cells. *Proc Natl Acad Sci USA* 103: 6196–6201